

Search for Dark Matter Annihilation to gamma-rays from SPT-SZ selected Galaxy Clusters

Siddhant Manna^{1,*} and Shantanu Desai^{1,†}

¹ Department of Physics, IIT Hyderabad Kandi, Telangana 502284, India

We search for dark matter annihilation from galaxy clusters in the energy range from 1-300 GeV using nearly 16 years of Fermi-LAT data. For this purpose, we use 350 galaxy clusters selected from the 2500 deg² SPT-SZ survey. We model the dark matter distribution using the NFW profile for the main halo along with the Einasto profile for the substructure. The largest signal is seen for the cluster SPT-CL J2021-5257 with a significance of around 3σ . The best-fit dark matter mass and annihilation cross-section for this cluster are equal to (60.0 ± 11.8) GeV and $\langle\sigma v\rangle = (6.0 \pm 0.6) \times 10^{-25} \text{ cm}^3 \text{s}^{-1}$ for the $\bar{b}b$ annihilation channel. However, this central estimate is in conflict with the limits on annihilation cross-section from dwarf spheroidal galaxies, and hence cannot be attributed to dark matter annihilation. Three other clusters show significance between $2 - 2.5\sigma$, whereas all the remaining clusters show null results. The most stringent 95% c.l. upper limit for the WIMP annihilation cross-section among all the clusters is from SPT-CL J0455-4159, viz. $\langle\sigma v\rangle = 6.44 \times 10^{-26} \text{ cm}^3 \text{s}^{-1}$ for $m_\chi = 10$ GeV and bb annihilation channel.

I. INTRODUCTION

The dark matter problem is one of the most outstanding unsolved problems in Astrophysics [1–4]. Although a large number of observations have pointed to a concordance model of the universe, which consists of about 25% cold dark matter [5], the identity of the cold dark matter candidate is unknown. One of the most well motivated and widely studied dark matter candidate is a weakly interacting massive particle (WIMP), which is a hypothetical stable particle, assumed to be a Majorana fermion with masses in the GeV-TeV range and weak-scale interactions [1, 2, 6]. The most well motivated WIMP candidate is the lightest supersymmetric particle, which is usually the neutralino [7]. Such a hypothetical particle has velocity averaged cross-section given by $\langle\sigma v\rangle \approx 3 \times 10^{-26} \text{ cm}^3 \text{ sec}^{-1}$. This cross-section yields the correct relic abundance, and enables the WIMP to decouple from the rest of the universe at non-relativistic velocities, thereby providing all the right properties needed for a cold dark matter candidate [1, 2, 8]. There are three kinds of experiments designed to look for signatures of WIMPs. The first type of search involves direct detection of WIMPs, where one looks for signatures of WIMP scattering with nuclei in an underground experiment [9]. The second search is referred to as indirect detection [10–12], where one looks for signatures of WIMP annihilation into secondary particles such as neutrinos [13], positrons [14], anti-protons [15], radio waves [16], and gamma-rays [17]. Finally, one can also look for dark matter signatures at particle colliders such as LHC [18].

In this work, we search for dark matter annihilation to gamma-rays using galaxy clusters. Galaxy clusters are the most massive gravitationally bound and virialized structures in the Universe and act as a unique laboratory to probe cosmology [19–21] and fundamental Physics [22–26]. Most of the mass of galaxy clusters (80-85%) is made up of dark matter [20]. Therefore, galaxy clusters are the largest reservoirs of dark matter and hence provide excellent targets in looking for signatures of dark matter annihilation [27].

The Fermi Gamma-ray Space Telescope which was launched in 2008 is currently the most sensitive telescope for gamma-ray astronomy at GeV energies. The Large Area Telescope (LAT) is one of the two instruments onboard this detector. Fermi-LAT is sensitive to high energy gamma rays from various astrophysical sources. It is a pair-conversion telescope that is sensitive to photons between the energy range of 20 MeV to more than 300 GeV [28] and is sensitive to dark matter annihilation if the dark matter is a WIMP with masses in the GeV range, since the photon energy from the annihilation products should be within the detector sensitivity.

A large number of searches have been done looking for dark matter annihilation in galaxy clusters using Fermi-LAT [29–41]. We briefly summarize these works. The very first search for dark matter annihilation from clusters was done using 11 months of Fermi-LAT data from six X-ray selected clusters in the HIFLUGCS catalog [29]. No significant gamma-ray detection was reported in this analysis. Subsequently, null results were reported based on a search from 49 galaxy clusters located at high galactic latitude using 2.8 years of Fermi-LAT data [30]. The most stringent upper limit from this analysis was from the Fornax cluster, given by $\langle\sigma v\rangle \lesssim (2 - 3) \times 10^{-25} \text{ cm}^3 \text{s}^{-1}$ for a WIMP mass of around 10 GeV [30]. Then, another search for dark

*Email:ph22resch11006@iith.ac.in

†Email:shntn05@gmail.com

matter annihilation and decay was done from eight nearby galaxy clusters (both individually and from a stacked analysis) using three years of Fermi-LAT data [31]. No evidence for gamma-ray emission at 3σ significance due to dark matter decay or annihilation was found from this analysis. Limits on the annihilation cross-section of around $10^{-25} \text{ cm}^3 \text{s}^{-1}$ were then obtained [31]. A similar search for dark matter annihilation from three nearby clusters, namely, VIRGO, Coma, Fornax was done using 45 months of Fermi-LAT data [32]. After removing the galactic and extragalactic gamma-ray foregrounds, a residual diffuse emission was found, which was attributed to additional point sources not included in the Fermi-LAT two-year catalog [32]. After accounting for these, no significant extended emission was detected from the aforementioned three clusters, and upper limits on the cross section for dark matter annihilation were obtained, which were more stringent than those obtained from Milky way dwarf galaxies [32]. Subsequently, Hektor et al. [33] found evidence for a double-peaked line at 110 and 130 GeV from 18 nearby brightest galaxy clusters with more than 3σ significance using 218 weeks of Fermi-LAT data, which they attributed to dark matter annihilation. However, this signal could not be confirmed in a subsequent follow-up analysis using enhanced exposure [34, 35]. A dedicated search for dark matter annihilation and point source emission from the VIRGO cluster was undertaken by the Fermi-LAT collaboration using three years of data, which reported null results [36]. This work then calculated limits on velocity averaged DM annihilation cross-section. Then in 2016, two independent groups did a search around the same time from the same set of 16 galaxy clusters from the HIFLUGCS sample with the largest J -factors, using five and seven years of data respectively [34, 35]. The first analysis did not find any significant excess in the energy range between 10 to 400 GeV and upper limits on the velocity averaged annihilation cross-section of around $3 \times 10^{-25} \text{ cm}^3 \text{s}^{-1}$ were obtained [34]. The second analysis found a line at 43 GeV after stacking with a significance of 3.0σ [35]. However, since the backgrounds were not fully understood, they did not claim a detection and set a conservative limit on the the velocity averaged annihilation cross-section [35]. A search for dark matter annihilation from galaxy groups (lower mass analogs of galaxy clusters) having large J -factors was carried out using 413 weeks of Fermi-LAT data [37]. No evidence for dark matter annihilations was found and thermal relic cross sections for dark matter masses below approximately 30 GeV to $b\bar{b}$ annihilation channel were excluded at 95% c.l. Then, another search for dark matter annihilation using 12 years of Fermi-LAT data from five nearby clusters (Centaurus, Coma, VIRGO, Fornax, and Perseus) reported null results and constraints on annihilation cross-section into three different channels were reported, which are between $10^{-26} - 10^{-23} \text{ cm}^3 \text{s}^{-1}$, depending on the WIMP mass [38]. A search for line and box-shaped signals was done in [39] using 7.1 years of Fermi-LAT data by stacking the same set of 16 clusters analyzed in [34, 35]. This work also found the 42 GeV line first reported in [35], although its significance was reduced. Consequently, 95% c.l. upper limits on the thermally averaged DM annihilation cross-section to photons between $10^{-27} - 10^{-25} \text{ cm}^3 \text{s}^{-1}$ were set [39]. About a year ago, Di Mauro et al. [40] (D23, hereafter) used 12 years of Fermi-LAT data to look for dark matter annihilation and decay from 49 clusters selected from the HIFLUGCS sample. The stacking analysis revealed a signal at $2.5\text{-}3.0\sigma$ significance. However, the best-fit values of the mass and cross-section are in tension with the null results obtained using dark matter searches from dwarf spheroidal galaxies. Therefore, it was concluded that the signal is most likely due to cosmic ray collisions with the gas and photon fields within the cluster [40]. Most recently, a constraint on the lifetime of very heavy dark matter with masses between 10^3 and 10^{11} GeV was set using 14 years of Fermi-LAT data, based on the analysis of seven clusters [41].

Complementary to the aforementioned target searches from individual clusters or a stacked analysis, a cross-correlation analysis between the 9-year Fermi-LAT diffuse gamma-ray map and four different galaxy cluster catalogs was done to look for dark matter annihilations, which reported null results [42]. In addition to galaxy clusters, a large number of works have also looked for dark matter annihilations and decay from Galactic center, dwarf spheroidal galaxies as well as Milky way satellites [43].

In this work, we look for WIMP dark matter annihilation from galaxy clusters detected by the South Pole Telescope (SPT) 2500 square deg survey, which have been detected using the Sunyaev-Zeldovich (SZ) effect [44], as a follow-up to our previous work which looked for point-source gamma-ray emission using 15 years of Fermi-LAT data [45]. We mainly follow the same methodology as D23. In our analysis, we have assumed a flat Λ CDM cosmology with $\Omega_m = 0.3$ and $H_0 = 70 \text{ kms}^{-1} \text{Mpc}^{-1}$. This manuscript is structured as follows. In Section II, we define the cluster catalog utilized in our manuscript. Section III provides a comprehensive description of the halo and subhalo modelling. Subsequently, in Section IV, we detail the analysis process employed in our study. Finally, in Section V, we present our results. The upper limits for all clusters can be found in Sect. VI. We present our conclusions in Section VII.

II. SPT-SZ CLUSTER CATALOG

For our analysis, we use the SZ selected cluster catalog detected by SPT, which provides a mass-limited sample. The SPT is a 10-meter telescope located at the South Pole that has imaged the sky at three different frequencies: 95 GHz, 150 GHz, and 220 GHz with an angular resolution of about 1 arcminute [46]. SPT completed a 2500 square degree survey between 2007 and 2011 to detect galaxy clusters using the SZ effect.

This survey detected 677 galaxy clusters with SNR greater than 4.5, corresponding to a mass threshold of $3 \times 10^{14} M_\odot$ up to redshift of 1.8 [47, 48]¹. The SPT cluster redshifts were obtained using a dedicated optical and infrared follow-up campaign from pointed imaging and spectroscopic observations [49, 50] in conjunction with data from optical imaging surveys such as the Blanco Cosmology Survey [51] and Dark Energy Survey [52]. We have previously done a search for gamma-rays induced due to astrophysical processes from 300 clusters from this sample, ranked according to M_{500}/z^2 [45]. Here, M_{500} denotes the total mass enclosed within a sphere with a mean density of 500 times the critical density of the universe at the cluster's redshift, and z represents the cluster's redshift [48]. In this work, we conduct a search for gamma-ray emission from dark matter annihilation for a sample of 350 galaxy clusters from the aforementioned catalog, after ranking them in decreasing order of their mass ratio, M_{500}/z^2 .

III. DARK MATTER ANALYSIS

The expected gamma-ray flux from the annihilation of WIMPs can be computed using the following equation [40, 53–56]²:

$$\frac{d\Phi_\gamma}{dE}(E, \Delta\Omega, \text{l.o.s}) = \frac{d\phi_\gamma}{dE}(E) \times J(\Delta\Omega, \text{l.o.s}). \quad (1)$$

Here, $\frac{d\Phi_\gamma}{dE}(E, \Delta\Omega, \text{l.o.s})$ is the WIMP dark matter induced differential gamma-ray flux per unit energy and solid angle as a function of energy (E), solid angle ($\Delta\Omega$), and line of sight (l.o.s.). The term $\frac{d\phi_\gamma}{dE}(E)$ is the gamma-ray energy spectrum per annihilation as a function of energy and represents the particle physics component of the gamma-ray flux, which encapsulates the spectral characteristics of the WIMP annihilation such as the properties of the dark matter particles and the annihilation channels involved. The differential gamma-ray flux is then computed as follows [40]:

$$\frac{d\phi_\gamma}{dE}(E) = \frac{\langle\sigma v\rangle}{8\pi m_\chi^2} \times \frac{dN_\gamma(E)}{dE}. \quad (2)$$

Here, $\frac{dN_\gamma(E)}{dE}$ denotes the WIMP photon spectrum, whose calculation is discussed in [56]. The mass of the WIMP, denoted as m_χ , determines the energy scale of the gamma rays produced during annihilation. The thermally-averaged annihilation cross-section, represented by $\langle\sigma v\rangle$, quantifies the likelihood of dark matter particles annihilating when they encounter each other. We can define the astrophysical J -factor $J(\Delta\Omega, \text{l.o.s})$ as the line-of-sight integral of the squared DM density profile over the solid angle at a given coordinate in the l.o.s. directions [40, 57]. The J -Factor can be mathematically written as:

$$J(\psi, \theta, \Delta\Omega) = \int_0^{\Delta\Omega} \int_{\text{l.o.s}} dl d\Omega \times \rho_{\text{tot}}(r)^2 \quad (3)$$

Here, $\Delta\Omega$ is the solid angle over which the integration is performed, $\rho_{\text{tot}}(r)$ is the total dark matter density profile as a function of the distance r from the centre of the system, and the integration is carried out along the line-of-sight (l.o.s.). The solid angle $\Delta\Omega$ is related to the integration angle α_{int} as:

$$\Delta\Omega = 2\pi(1 - \cos \alpha_{\text{int}}) \quad (4)$$

where α_{int} is the angle between the line-of-sight and the direction pointing toward the centre of the cluster. We have chosen α_{int} to be 0.2° similar to size of the spatial bins used for the analysis. In the context of modelling the dark matter distribution within galaxy clusters, a common approach is to consider the total dark matter density profile as the sum of two components [40]:

$$\rho_{\text{tot}}(r) = \rho_{\text{main}}(r) + \langle\rho_{\text{subs}}\rangle(r) \quad (5)$$

The first term on the right-hand side, $\rho_{\text{main}}(r)$, represents the smooth, large-scale distribution of dark matter within the main halo of the galaxy clusters, whereas the second term ($\langle\rho_{\text{subs}}\rangle(r)$) accounts for the contribution of the population of subhalos within the main halo of the galaxy cluster, according to the standard Λ CDM cosmological model [58–60]. Subhalos are smaller-scale dark matter structures that are gravitationally bound

¹ https://pole.uchicago.edu/public/data/sptsz-clusters/2500d_cluster_sample_Bocquet19.fits

² We follow the same notation as D23

within the larger main halo [61, 62]. Since individual subhalos cannot be resolved, we use a statistical description of the subhalos to calculate the annihilation signal.

In the next subsection, we discuss the modelling of the smooth halo and subhalo dark matter component. This modelling process allows us to calculate the expected fluxes arising from DM annihilation within these clusters.

A. Modelling the Main Halo

For our work, we modelled the main smooth dark matter halo using the Navarro-Frenk-White (NFW) density profile [63–65], which can be written as follows:

$$\rho(r) = \frac{\rho_0}{\frac{r}{r_s} \left(1 + \frac{r}{r_s}\right)^2} \quad (6)$$

Here, ρ_0 is the characteristic dark matter density for the NFW profile and r_s is the NFW scale radius. The NFW profile is usually reparameterized in terms of the halo mass and concentrations as described below.

The first step in obtaining the halo concentration involves choosing a mass proxy. For this purpose, we use M_{200} , which is the cluster mass at a spherical overdensity, which is about 200 times the critical density of the Universe. We have obtained M_{200} values from the SPT-SZ 2500 square-degree catalogue [48, 66]. In accordance with [40, 67], we define the virial radius, R_{200} which can be estimated from M_{200} as follows:

$$R_{200} = \left(\frac{3M_{200}}{4\pi\Delta_{200}\rho_{crit}} \right)^{1/3} \quad (7)$$

where Δ_{200} is the overdensity factor, which is 200 in this case. The critical density, ρ_{crit} , is calculated using the Hubble parameter $H(z)$, which is the rate at which the universe expands and is given by:

$$\rho_{crit} = \frac{3H^2(z)}{8\pi G} \quad (8)$$

where $H(z) \equiv H_0\sqrt{\Omega_M(1+z)^3 + 1 - \Omega_M}$ for flat Λ CDM. We now introduce the halo concentration (c_{200}) defined as $c_{200} \equiv \frac{R_{200}}{r_s}$.

Next, we need to determine c_{200} for every cluster. Although, an extensive weak lensing campaign has been undertaken for SPT clusters for precise mass measurements and cosmological analyses [48] (and references therein), no concentration measurements are available on a per cluster basis. Therefore, we use the concentration-mass ($c - M$) relations from cosmological simulations for modelling the dark matter halo. Similar to D23, we use the concentration-mass relations from [68], which have been shown to match the observational results across a wide range of halo masses from dwarf spheroidal galaxies to galaxy clusters. This mass-concentration relation allows us to obtain c_{200} from the estimated M_{200} for every SPT cluster.

The scale density ρ_0 in Eq. 6 can be computed from c_{200} as follows:

$$\rho_0 = \frac{2\Delta_{200}\rho_{crit}c_{200}}{3f(c_{200})}, \quad (9)$$

where $f(c_{200})$ is given by:

$$f(c_{200}) = \frac{2}{(c_{200}^2)} \left[\ln(1 + c_{200}) - \frac{c_{200}}{1 + c_{200}} \right]. \quad (10)$$

B. Modelling the subhalo

Structure formation follows a bottom-up hierarchical process in the standard Λ CDM cosmological model [69]. This means that the smallest structures, known as subhalos, form first. Over time, these subhalos merge and accrete matter, leading to the formation of larger and larger structures, such as galaxy groups and clusters [62]. Galaxy clusters are expected to host a large number of subhalos. We shall now discuss the modelling of the subhalo population along the same lines as D23. The subhalos account for the smaller-scale clumps and inhomogeneities within the halo.

For this purpose, we use the CLUMPY v3 software [53–55, 70]³ where the Einasto profile [71] is used to describe the density distribution of subhalos. The distribution of subhalos within a main halo is influenced by both their distance from the host center and also their mass. The total distribution of subhalos can be expressed as the product of three uncorrelated probability distribution functions (PDFs) and a normalization factor [40, 53, 54, 70] as follows:

$$\frac{d^3N}{dVdMdC} = N_{tot} \frac{dP_V(R)}{dV} \times \frac{dP_M(M)}{dM} \times \frac{dP_c}{dc}(M, c). \quad (11)$$

In the above equation, N_{tot} refers to the expected number of subhalos within the virial radius of main halo, and P_i with $i = V, M, c$ is the probability distribution in each of the respective domains, normalized to 1. Here, V corresponds to the volume of the main halo, M pertains to the distribution of subhalo masses, and c represents the subhalo concentration. Although, numerical cosmological simulations have significantly advanced our understanding of halo substructures [62], several questions still remain unresolved, such as the minimum mass for clump formation [27], the effects of tidal stripping on subhalo survival [72], and the exact shape of the subhalo DM density profiles [73]. These uncertainties impact the calculation of the DM-induced γ -ray flux. In this work, we follow the same prescription as D23 to account for each of the terms in Eq. 11, which we describe below:

- Spatial distribution PDF ($dP_V(R)/dV$): Since the main halo is spherically symmetric, the distribution of subhalos within it depends only on their distance from the central point of the host halo. It describes the probability of finding a subhalo at a given distance from the host halo centre and provides the spatial distribution of substructures in a host halo, which in our study are the galaxy clusters. We modelled it using the Einasto profile.
- Mass distribution PDF ($dP_m(M)/dM$): Subhalo mass function can be defined as:

$$\frac{dP_M}{dM} \propto M^{-\alpha}, \quad (12)$$

We have used $\alpha = 1.9$ in our study, similar to [40, 74]. It represents a more conservative approach as it implies lesser number of subhalos. It also aligns with the results reported in [62].

- Concentration distribution PDF ($dP_c(M, c)/dc$): As reported in [72–77], subhalos experience tidal forces that generally result in significant mass loss, particularly in their outer regions. As a result, subhalos tend to be more concentrated compared to the main halos with equivalent mass [78–80]. We have used $(c - M)$ relation defined in [78] for the subhalos, similar to D23. It accounts for the spatial dependence of the subhalos within the main halos.

In order to account for the uncertainties in the above factors, D23 considered three benchmark models. In this work, we choose the parameters corresponding to the MED model in D23. The smallest subhalo mass is assumed to be $10^{-6}M_\odot$ and the largest subhalo mass is 0.01% of the halo mass. Finally, we specify the number of multilevel substructures to be two, as in D23. All the relevant properties used for modelling of dark matter halos and subhalos are summarized in Table I. The distribution of J -factors for SPT-SZ clusters using this model for the dark matter halo and substructure can be found in Figure 1. The values for individual clusters are listed in Table II.

IV. FERMI-LAT ANALYSIS

A. Data selection

We conducted our search using 15.7 years of Fermi-LAT data from August 5, 2008 to April 1, 2024, (MET 239587201–733622405). For each cluster, a circular region of interest (ROI) with a 10° radius centered on the cluster was defined. The analysis was restricted to events within this ROI with energies ranging from 1 GeV to 300 GeV with 37 logarithmic energy bins per decade. We excluded lower energy events (below 1 GeV) due to the degraded Point Spread Function (PSF) at those energies [81, 82]. The binned maximum-likelihood method was implemented using the P8R3_ULTRACLEANVETO_V3 instrument response functions (IRFs) and Pass 8 ULTRACLEANVETO ("FRONT+BACK") class events [83].

³ https://clumpy.gitlab.io/CLUMPY/v3.1.1/_downloads/975332ce6631f0956830ed27431f3b25/CLUMPY_v2018.06.CPC.tar.gz

TABLE I: Parameters used for modelling the dark matter halo and subhalo.

Parameter	Value
Smallest subhalo mass	$10^{-6} M_{\odot}$
Biggest subhalo mass	0.01 % of host mass
Number of multilevel substructures	2
Mass-concentration model for Halos	[68]
Mass-concentration model for subhalos	[78]
dP/dV profile of subhalo distribution in host	EINASTO
Slope of power law subhalo mass spectrum dP/dM	1.9
Fraction of host halo mass bound in subhalos	0.1
Branching Ratio Channel	$b\bar{b}, \tau^+\tau^-$
Spectrum Model	[56]
Dark Matter Particle	Majorana

We also applied the filters, `DATA_QUAL > 0` and `LAT_CONFIG == 1`, which were utilized to eliminate low-quality data. The rock angle was constrained to `abs(rock_angle) < 52°` and `|b| < 20°` to mitigate particle contamination. To reduce atmospheric interference, a zenith angle cut of 90° was imposed on the events. We also removed all clusters within 20° of the galactic plane. The spatial binning of the data was performed at a resolution of 0.2° pixels, which helps to reduce noise and improve the signal-to-noise ratio. Our background model incorporated all the gamma-ray sources from the fourth Fermi-LAT catalogue (4FGL-DR4) [84], encompassing both point-like and extended sources. To account for the pervasive, low-intensity gamma-ray emission from the Milky Way galaxy itself (diffuse emission), we employed the Galactic diffuse emission model (`gll_iem_v07.fits`). Additionally, an isotropic component (`iso_P8R3_ULTRACLEANVETO_V3_v1.txt`) is included to represent the isotropic gamma-ray background from various unresolved extragalactic sources. The analysis pipeline employed the `FermiTools` (v2.2.0) software within the Fermi Science Support Center's Fermibottle Docker environment [85].

B. Analysis Method

Our analysis followed the standard binned-likelihood method developed by the Fermi-LAT collaboration for likelihood calculations and model fitting [28]. We incorporated sources from the 4FGL catalog up to 10° beyond the defined region of interest into our model, freezing all their parameters to the catalog values. This was done to minimize bias from the potential presence of bright sources outside the targeted area and to account for the LAT's poor point spread function (PSF) at low energies around 0.1 GeV [38, 45]. In the first phase of the analysis, the spectral parameters for all the free sources were determined. During the second phase, we then fixed the spectral parameters of all sources, except for the normalizations to their best-fit values. Then, we included a template for potential dark matter annihilation in the model, which we modeled as a diffuse source with a spatial distribution proportional to the J -factor calculated using CLUMPY and specified in Table II. The spectral component of the signal was given by the spectrum of annihilating dark matter for the specified channel utilizing the `DMFitFunction` [86] within `FermiTools` similar to [38].

We used the `gtapps` tool for our analysis and employed the Maximum Likelihood Estimation (MLE) technique to identify the model parameters that best match the source's spectrum and location. The `gtlike` tool performs a binned likelihood analysis on Fermi-LAT gamma-ray data. It achieves this by comparing a model of the gamma-ray sky with actual observations and calculating the likelihood that the model explains the data. To identify gamma-ray sources and assess their significance, we employ the Test Statistic (TS) calculated using the `gttsmap` tool. This statistic, defined as [87]

$$TS = -2 \ln(L_{max,0}/L_{max,1}), \quad (13)$$

compares the likelihoods of two scenarios: where $L_{max,0}$ is a model without the source (null hypothesis) and $L_{max,1}$ is a model including the source at a specific location (alternative hypothesis). Wilks' theorem tells us that for high photon counts, the TS for the null hypothesis behaves similar to a chi-squared distribution [88]. The detection significance is thereby nominally obtained by taking the square root of TS. However, D23 has shown using simulations, that for the null hypothesis the TS statistics has larger tails, which are not expected in the χ^2 distribution. Therefore, the actual detection significance would be expected to be smaller than the square root of TS. Nevertheless, we shall quote the significance as the square root of TS for our results. We note that the same TS statistic is also used in neutrino and soft gamma-ray astrophysics to evaluate the significance of detections [89, 90].

V. RESULTS

We conducted the analysis for the clusters in our sample using the $b\bar{b}$ and $\tau^+\tau^-$ annihilation channels in the energy range between 1-300 GeV. The TS values for all the 350 galaxy clusters (for the $b\bar{b}$ annihilation channel) can be found in Table II. Among all the clusters, SPT-CL J2021-5257 shows the maximum TS value of 9.2, corresponding to 3.03σ significance. The corresponding TS map for this cluster is shown in Figure 2. We also performed the analysis for SPT-CL J2021-5257 by extending the lower energy range to 100 MeV, and found that the TS value decreases to 7 corresponding to 2.6σ significance. Other clusters, such as SPT-CL J2012-5649, SPT-CL J0124-5937, and SPT-CL J2300-5331 show TS values corresponding to $\sim 2 - 2.5\sigma$ significance, suggesting a weaker detection significance. The variation of TS values as a function of the dark matter mass for the aforementioned clusters with significance $>= 2\sigma$ can be found in Figure 3 for $b\bar{b}$ annihilation channel. The best fit WIMP mass for SPT-CL J2021-5257 is found to be (60.0 ± 11.8) GeV, whereas the best-fit value of $\langle\sigma v\rangle = (6.0 \pm 0.6) \times 10^{-25} \text{cm}^3 \text{s}^{-1}$ for this cluster assuming a $b\bar{b}$ annihilation channel. For SPT-CL J2012-5649, SPT-CL J0124-5937, and SPT-CL J2300-5331, the best-fit masses were found to be (90.0 ± 4.5) GeV, (42.5 ± 5.7) GeV, and (65.0 ± 3.8) GeV, respectively. The corresponding best-fit values of $\langle\sigma v\rangle$ for the $b\bar{b}$ channel were $(5.9 \pm 0.5) \times 10^{-24} \text{cm}^3 \text{s}^{-1}$, $(9.0 \pm 0.3) \times 10^{-25} \text{cm}^3 \text{s}^{-1}$ and $(3.5 \pm 0.2) \times 10^{-25} \text{cm}^3 \text{s}^{-1}$, respectively. The best-fit dark matter mass for SPT-CL J2021-5257 for the $\tau^+\tau^-$ annihilation channel is found to be (15.3 ± 4.1) GeV, whereas the best-fit annihilation cross-section is given by $\langle\sigma v\rangle = (3.5 \pm 0.9) \times 10^{-25} \text{cm}^3 \text{s}^{-1}$. Similarly, for SPT-CL J2012-5649, SPT-CL J0124-5937, and SPT-CL J2300-5331 we found the best-fit mass as (24.0 ± 1.5) , (15.0 ± 2.8) , and (22.0 ± 2.1) GeV, respectively, whereas the best-fit values of $\langle\sigma v\rangle$ are equal to $(5.0 \pm 0.4) \times 10^{-24} \text{cm}^3 \text{s}^{-1}$, $(6.3 \pm 0.8) \times 10^{-25} \text{cm}^3 \text{s}^{-1}$ and $(2.8 \pm 0.4) \times 10^{-25} \text{cm}^3 \text{s}^{-1}$, respectively for this annihilation channel. The variation of TS value with the WIMP mass for the $\tau^+\tau^-$ annihilation channel for all the four clusters can be found in Fig. 4. We also show how TS varies with other subhalo models and uncertainties on J -factors in Appendix A, B, and C.

As pointed out in D23, these values are in conflict with the upper limits obtained from null searches for dark matter annihilation from Milky Way dwarf spheroidal galaxies, whose 95% c.l. limits on the velocity-averaged annihilation cross-section are around $10^{-26} \text{cm}^3/\text{sec}$ [91]. Therefore, although our significance does not cross the 5σ threshold, these enhanced TS values corresponding to $(2-3)\sigma$ significance cannot be by-products of dark matter annihilation. Furthermore, after considering the look elsewhere effect, given that we have analyzed 350 galaxy clusters [92], the global p -value for the cluster with the highest TS value of around 9.2, is equal to 0.47, which is consistent with the expected background. However, if we ignore the look elsewhere effect, and in case the significance increases with additional exposure, then one explanation is that this signal could be due to some astrophysical process resulting from cosmic interactions with gas and photons in the intracluster medium, as pointed out in D23.

Therefore, we calculate upper limits for the dark matter annihilation cross-section for these clusters. For the aforementioned four clusters, we show the 95% c.l. upper limits on the annihilation cross-section as a function of WIMP mass for the $b\bar{b}$ annihilation channel in Figure 5 and for the $\tau^+\tau^-$ channel in Figure 6. Our upper limits are mostly in agreement with other works, which have obtained upper limits on the annihilation cross-section [29, 32, 38, 40]. A compilation of upper limits for all the remaining galaxy clusters analyzed in this work can be found in Table III, as discussed in Sect. VI. Among all the clusters with significance $>= 2\sigma$, we found the most stringent limit for SPT-CL J2300-5331, viz. $\langle\sigma v\rangle = 8.85 \times 10^{-26} \text{cm}^3 \text{s}^{-1}$ for $m_\chi = 10$ GeV considering the $b\bar{b}$ annihilation channel, and $\langle\sigma v\rangle = 10.0 \times 10^{-26} \text{cm}^3 \text{s}^{-1}$ for $m_\chi = 10$ GeV and considering the $\tau^+\tau^-$ annihilation channel. We note that one of the clusters with $>= 2\sigma$ significance is SPT-CL J2012-5649 (TS = 6.4), which is spatially coincident with the merging cluster Abell 3667. This cluster was detected with the highest significance ($> 6\sigma$) in our previous work on gamma-ray searches using a point source template [45].

All other clusters have significance less than 3σ . These include the merging clusters in our sample such as Bullet Cluster (SPT-CL J0658-5556) and El Gordo Cluster (SPT-CL J0102-4915) with TS values of 1.5 and 1.9, respectively, corresponding to no significant excess. Since the last 100 clusters in our sample (sorted according to M_{500}/z^2) showed no significance we restricted our analysis to 350 clusters and did not go beyond that.

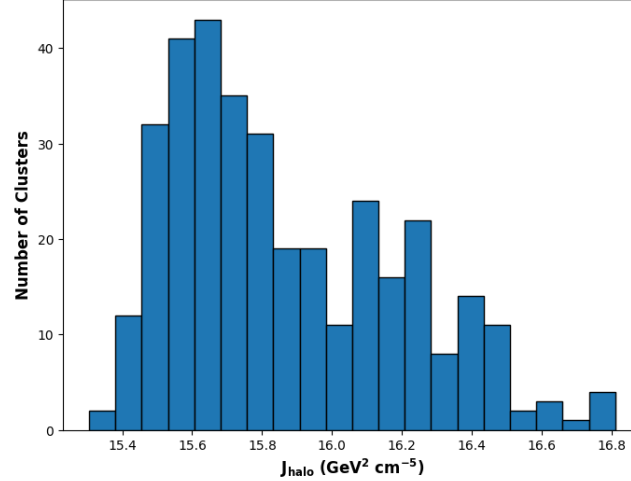


FIG. 1: Distribution of J -Factors for all the 350 SPT-SZ clusters used in our analysis.

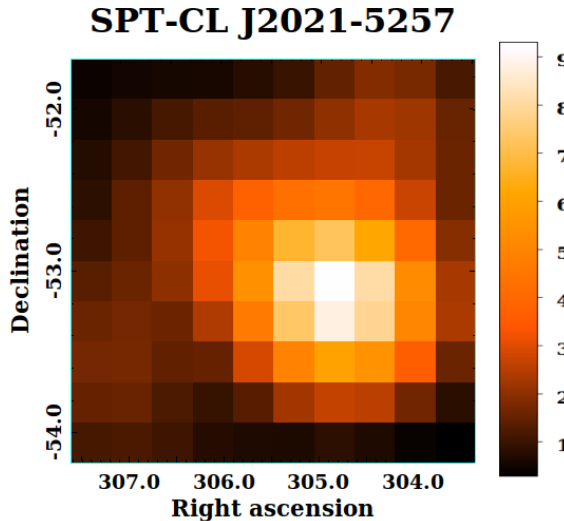


FIG. 2: Gaussian kernel smoothed ($\sigma = 1.5$) TS map of the SPT-CL J2021-5257 cluster (left) and TS map scale (right) generated using `gttsmap` in the energy band 1 – 300 GeV. We used 0.2-pixel resolution for the spatial binning.

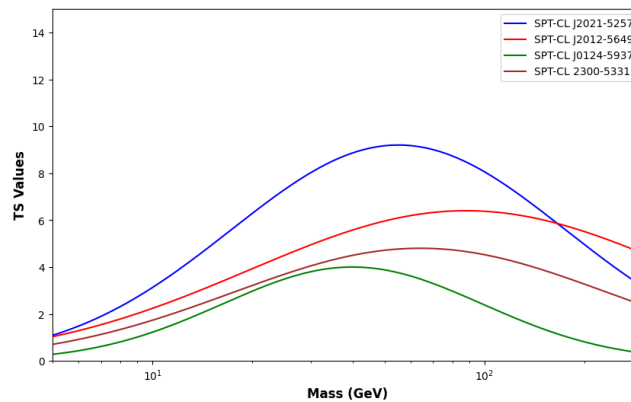


FIG. 3: TS as a function of the WIMP mass for clusters with $\text{TS} \geq 4$ for the $b\bar{b}$ annihilation channel.

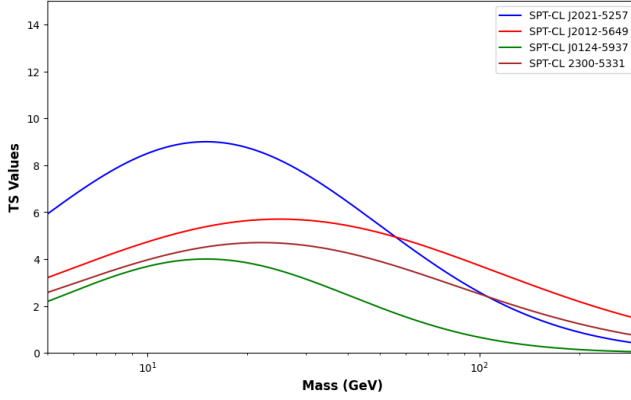


FIG. 4: Similar to Figure 3 but here we show TS as a function of WIMP mass for the $\tau^+\tau^-$ annihilation channel.

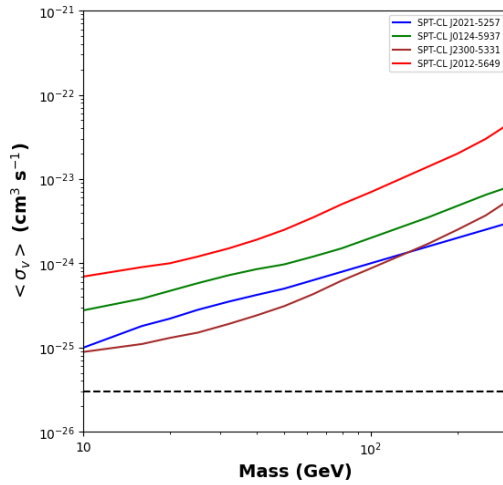


FIG. 5: 95 % c.l. upper limits on the annihilation cross-section of WIMP dark matter for the $b\bar{b}$ annihilation channel, considering the presence of substructures in the galaxy clusters with $TS \geq 4$. The black solid line indicates the canonical thermal cross-section of $3 \times 10^{-26} \text{ cm}^3 \text{s}^{-1}$.

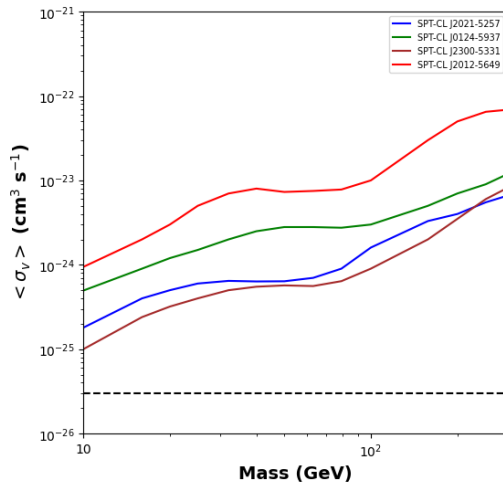


FIG. 6: Similar to Figure 4 but here we show the 95% c.l. upper limits for $\tau^+\tau^-$ annihilation channel similar to [40].

TABLE II: The SPT-SZ galaxy clusters along with their coordinates, virial mass, redshifts, normalization, where $\rho_s = \rho_0/4$, scale radius, J values and TS Values for $b\bar{b}$ annihilation channel . The clusters are ranked in decreasing order of their M_{500}/z^2 values. All clusters with TS $>= 4$ are highlighted in bold. We have integrated out to the size of the spatial bin which is 0.2° .

Cluster Name	R.A.	Dec.	M_{200}	z	ρ_s	r_s	J_{halo}	TS Values
	($^\circ$)	($^\circ$)	$\times 10^{14} M_\odot/h$		$M_\odot \text{ Kpc}^{-3}$	(Kpc)	$\text{GeV}^2 \text{ cm}^{-5}$	
SPT-CL J2012-5649	303.11	-56.83	7.22	0.06	2.97×10^5	416.3	6.45×10^{16}	6.4
SPT-CL J0431-6126	67.84	-61.44	7.2	0.06	2.97×10^5	416.0	6.00×10^{16}	1.5
SPT-CL J2313-4243	348.5	-42.73	6.71	0.06	2.98×10^5	405.8	5.85×10^{16}	2.0
SPT-CL J2009-4518	302.45	-45.31	6.23	0.06	2.99×10^5	395.2	5.25×10^{16}	1.9
SPT-CL J2201-5956	330.47	-59.94	14.03	0.1	2.92×10^5	523.0	5.60×10^{16}	0.8
SPT-CL J0328-5541	52.17	-55.7	8.18	0.08	2.95×10^5	435.0	4.55×10^{16}	3.5
SPT-CL J2217-6509	334.49	-65.15	7.99	0.1	2.96×10^5	431.3	4.00×10^{16}	0.8
SPT-CL J2249-6426	342.43	-64.43	7.22	0.09	2.97×10^5	416.3	3.85×10^{16}	1.6
SPT-CL J0145-5301	26.26	-53.03	8.43	0.12	2.95×10^5	439.6	3.50×10^{16}	2.7
SPT-CL J0645-5413	101.37	-54.22	15.33	0.16	2.92×10^5	538.8	3.75×10^{16}	1.5
SPT-CL J0500-5116	75.24	-51.27	6.66	0.11	2.98×10^5	404.6	3.20×10^{16}	3.2
SPT-CL J2055-5456	314.0	-54.94	8.48	0.14	2.95×10^5	440.5	3.10×10^{16}	2.5
SPT-CL J0628-4143	97.2	-41.73	12.88	0.18	2.92×10^5	508.3	3.20×10^{16}	2.9
SPT-CL J0404-6510	61.05	-65.18	5.74	0.12	3.00×10^5	383.9	2.80×10^{16}	2.5
SPT-CL J0641-5001	100.46	-50.02	5.85	0.12	2.99×10^5	386.4	2.75×10^{16}	3.1
SPT-CL J0411-6340	62.86	-63.68	7.29	0.14	2.97×10^5	417.7	2.85×10^{16}	2.6
SPT-CL J0145-6033	26.3	-60.56	10.89	0.18	2.93×10^5	480.1	2.83×10^{16}	0.9
SPT-CL J2021-5257	305.48	-52.95	6.36	0.14	2.99×10^5	398.1	2.75×10^{16}	9.2
SPT-CL J0638-5358	99.7	-53.97	17.38	0.23	2.92×10^5	561.5	3.10×10^{16}	2.2
SPT-CL J2012-4130	303.0	-41.5	7.01	0.15	2.97×10^5	412.1	2.55×10^{16}	1.3
SPT-CL J0516-6312	79.09	-63.21	5.98	0.14	3.00×10^5	389.6	2.50×10^{16}	3.0
SPT-CL J2259-5617	345.0	-56.29	7.09	0.15	2.97×10^5	413.6	2.63×10^{16}	2.0
SPT-CL J0027-5015	6.82	-50.25	6.34	0.15	2.99×10^5	397.8	2.50×10^{16}	2.5
SPT-CL J0525-4715	81.46	-47.26	11.0	0.19	2.93×10^5	481.7	2.73×10^{16}	2.8
SPT-CL J2254-5805	343.59	-58.09	6.72	0.15	2.98×10^5	405.9	2.50×10^{16}	1.9
SPT-CL J0537-6504	84.35	-65.07	10.67	0.2	2.93×10^5	476.9	2.55×10^{16}	2.8
SPT-CL J0658-5556	104.63	-55.95	23.99	0.3	2.94×10^5	623.2	3.00×10^{16}	1.7
SPT-CL J0510-4519	77.58	-45.33	10.55	0.2	2.93×10^5	474.9	2.50×10^{16}	0.8
SPT-CL J0637-4829	99.35	-48.49	10.42	0.2	2.93×10^5	472.9	2.45×10^{16}	2.2
SPT-CL J2134-4238	323.5	-42.64	9.44	0.2	2.94×10^5	457.1	2.40×10^{16}	2.6
SPT-CL J0051-4834	12.79	-48.58	8.61	0.19	2.94×10^5	442.8	2.40×10^{16}	2.4
SPT-CL J0317-4849	49.45	-48.83	6.08	0.16	2.99×10^5	391.9	2.15×10^{16}	1.6
SPT-CL J2023-5535	305.84	-55.59	11.87	0.23	2.92×10^5	494.5	2.35×10^{16}	1.9
SPT-CL J0232-4421	38.07	-44.35	17.49	0.28	2.92×10^5	562.6	2.50×10^{16}	2.3
SPT-CL J0216-4816	34.07	-48.28	6.11	0.17	2.99×10^5	392.4	2.10×10^{16}	2.1
SPT-CL J2025-5117	306.48	-51.29	10.05	0.22	2.93×10^5	467.1	2.35×10^{16}	2.2
SPT-CL J0010-5112	2.74	-51.21	5.87	0.17	3.00×10^5	386.9	2.05×10^{16}	1.8
SPT-CL J2254-6314	343.51	-63.25	9.02	0.21	2.94×10^5	450.1	2.18×10^{16}	1.5
SPT-CL J2248-4431	342.19	-44.53	24.65	0.35	2.95×10^5	628.6	2.55×10^{16}	1.1
SPT-CL J0013-4621	3.47	-46.36	5.88	0.18	3.00×10^5	387.1	2.00×10^{16}	2.9
SPT-CL J2020-4646	305.19	-46.77	6.33	0.19	2.99×10^5	397.5	1.95×10^{16}	1.5
SPT-CL J0504-4929	76.01	-49.49	6.82	0.2	2.98×10^5	408.2	1.95×10^{16}	1.3
SPT-CL J0225-4155	36.48	-41.92	7.88	0.22	2.96×10^5	429.4	2.00×10^{16}	1.5
SPT-CL J0458-5741	74.6	-57.7	5.82	0.19	3.00×10^5	385.8	1.85×10^{16}	1.9
SPT-CL J2241-4236	340.47	-42.6	6.4	0.2	2.99×10^5	399.1	1.90×10^{16}	2.2
SPT-CL J0108-4341	17.13	-43.69	5.74	0.19	3.00×10^5	383.9	1.85×10^{16}	1.9
SPT-CL J0124-5937	21.2	-59.63	7.02	0.21	2.97×10^5	412.3	1.88×10^{16}	4.0
SPT-CL J0256-4736	44.24	-47.61	8.02	0.23	2.96×10^5	432.0	1.85×10^{16}	2.1
SPT-CL J0653-5744	103.33	-57.75	8.68	0.24	2.94×10^5	444.0	1.90×10^{16}	1.1
SPT-CL J2211-4833	332.83	-48.56	8.33	0.24	2.95×10^5	437.7	1.85×10^{16}	2.4
SPT-CL J0118-5638	19.54	-56.63	6.24	0.21	2.99×10^5	395.5	1.80×10^{16}	1.7
SPT-CL J0651-4037	102.82	-40.63	7.8	0.24	2.96×10^5	427.9	1.85×10^{16}	3.7
SPT-CL J2121-6335	320.43	-63.58	6.34	0.22	2.99×10^5	397.7	1.75×10^{16}	1.8
SPT-CL J0001-6258	0.4	-62.98	5.85	0.21	2.99×10^5	386.5	1.65×10^{16}	1.1
SPT-CL J0235-5121	38.95	-51.35	10.03	0.28	2.93×10^5	466.8	1.74×10^{16}	1.2

TABLE II – continued

SPT-CL J2005-5635	301.34	-56.59	5.58	0.21	3.00×10^5	380.0	1.74×10^{16}	2.6
SPT-CL J2254-4620	343.59	-46.34	9.05	0.27	2.94×10^5	450.5	1.70×10^{16}	1.0
SPT-CL J0549-6205	87.33	-62.09	18.2	0.38	2.92×10^5	570.1	1.88×10^{16}	1.1
SPT-CL J0516-5430	79.15	-54.51	10.92	0.3	2.93×10^5	480.7	1.90×10^{16}	3.8
SPT-CL J2031-4037	307.97	-40.62	14.64	0.34	2.92×10^5	530.5	1.80×10^{16}	1.9
SPT-CL J0225-4327	36.3	-43.46	6.41	0.23	2.98×10^5	399.3	1.64×10^{16}	2.2
SPT-CL J0040-4407	10.2	-44.13	15.23	0.35	2.92×10^5	537.5	1.82×10^{16}	1.5
SPT-CL J0620-4715	95.1	-47.26	6.37	0.23	3.00×10^5	398.3	1.64×10^{16}	1.7
SPT-CL J2019-5642	304.77	-56.71	6.11	0.23	2.99×10^5	392.5	1.60×10^{16}	3.2
SPT-CL J0249-5658	42.41	-56.98	6.33	0.24	3.00×10^5	397.4	1.56×10^{16}	2.1
SPT-CL J0603-4714	90.99	-47.24	8.58	0.27	2.95×10^5	442.4	1.72×10^{16}	2.4
SPT-CL J0601-4122	90.5	-41.37	5.9	0.23	2.99×10^5	387.6	1.50×10^{16}	2.5
SPT-CL J2138-6008	324.51	-60.13	11.18	0.32	2.93×10^5	484.5	1.58×10^{16}	0.8
SPT-CL J2032-5627	308.08	-56.46	8.76	0.28	2.94×10^5	445.4	1.55×10^{16}	1.5
SPT-CL J2223-5015	335.81	-50.27	6.13	0.24	2.99×10^5	392.9	1.56×10^{16}	2.7
SPT-CL J0412-5106	63.23	-51.11	5.99	0.24	3.00×10^5	389.7	1.50×10^{16}	2.3
SPT-CL J2120-4016	320.14	-40.27	6.35	0.25	2.99×10^5	397.9	1.55×10^{16}	2.7
SPT-CL J2219-5708	334.96	-57.14	9.66	0.30	2.93×10^5	460.9	1.66×10^{16}	3.0
SPT-CL J2300-5331	345.18	-53.52	6.78	0.26	2.98×10^5	407.2	1.50×10^{16}	4.8
SPT-CL J2027-4240	306.93	-42.67	5.96	0.25	2.99×10^5	389.0	1.44×10^{16}	2.4
SPT-CL J0555-6406	88.87	-64.1	11.79	0.35	2.92×10^5	493.3	1.50×10^{16}	1.3
SPT-CL J0311-6354	47.83	-63.91	7.83	0.28	2.96×10^5	428.4	1.46×10^{16}	2.1
SPT-CL J0129-6432	22.43	-64.54	10.34	0.33	2.93×10^5	471.7	1.50×10^{16}	2.2
SPT-CL J0505-6145	76.4	-61.75	7.85	0.29	2.96×10^5	428.7	1.38×10^{16}	1.2
SPT-CL J0133-6434	23.41	-64.57	9.59	0.32	2.94×10^5	459.7	1.40×10^{16}	1.3
SPT-CL J2325-4111	351.3	-41.2	11.62	0.36	2.92×10^5	490.8	1.35×10^{16}	0.0
SPT-CL J0438-5419	69.57	-54.32	16.08	0.42	2.92×10^5	547.3	1.45×10^{16}	2.8
SPT-CL J0405-4916	61.49	-49.27	7.75	0.30	2.96×10^5	426.8	1.28×10^{16}	1.0
SPT-CL J2344-4224	356.15	-42.41	5.65	0.26	3.00×10^5	381.7	1.28×10^{16}	2.1
SPT-CL J0150-4511	27.65	-45.19	8.06	0.31	2.96×10^5	432.7	1.30×10^{16}	2.0
SPT-CL J0041-4428	10.25	-44.48	9.29	0.33	2.94×10^5	454.6	1.25×10^{16}	0.7
SPT-CL J0214-4638	33.7	-46.65	7.46	0.30	2.96×10^5	421.2	1.32×10^{16}	2.8
SPT-CL J0143-4452	25.89	-44.87	6.06	0.27	2.99×10^5	391.3	1.30×10^{16}	2.5
SPT-CL J0655-5541	103.91	-55.69	6.74	0.29	2.98×10^5	406.3	1.26×10^{16}	2.1
SPT-CL J2101-5542	315.31	-55.7	5.77	0.27	3.00×10^5	384.5	1.28×10^{16}	2.5
SPT-CL J0440-4657	70.23	-46.97	7.7	0.31	2.96×10^5	426.0	1.20×10^{16}	0.7
SPT-CL J0106-5943	16.62	-59.72	9.85	0.35	2.93×10^5	463.9	1.30×10^{16}	1.5
SPT-CL J2130-6458	322.73	-64.98	7.98	0.32	2.96×10^5	431.3	1.25×10^{16}	2.0
SPT-CL J0439-4600	69.81	-46.01	8.55	0.33	2.95×10^5	441.8	1.28×10^{16}	2.9
SPT-CL J2011-5725	302.85	-57.42	6.04	0.28	2.99×10^5	390.9	1.30×10^{16}	3.4
SPT-CL J0348-4515	57.07	-45.25	9.75	0.36	2.93×10^5	462.2	1.26×10^{16}	2.5
SPT-CL J0304-4921	46.06	-49.36	11.67	0.39	2.92×10^5	491.6	1.20×10^{16}	2.0
SPT-CL J0455-4159	74.0	-41.99	6.07	0.29	2.99×10^5	391.6	1.35×10^{16}	3.6
SPT-CL J2223-5227	335.87	-52.47	6.07	0.29	2.99×10^5	391.5	1.10×10^{16}	0.8
SPT-CL J2115-4659	318.8	-46.99	6.46	0.30	2.98×10^5	400.2	1.08×10^{16}	1.3
SPT-CL J2016-4954	304.01	-49.91	5.93	0.29	3.00×10^5	388.3	1.10×10^{16}	2.0
SPT-CL J0522-4818	80.57	-48.3	6.2	0.30	2.99×10^5	394.5	1.25×10^{16}	3.2
SPT-CL J0151-5654	27.79	-56.91	5.84	0.29	3.00×10^5	386.2	1.20×10^{16}	2.8
SPT-CL J0234-5831	38.68	-58.52	12.32	0.42	2.92×10^5	500.7	1.20×10^{16}	2.4
SPT-CL J0114-4123	18.68	-41.4	10.87	0.39	2.93×10^5	479.9	1.24×10^{16}	2.8
SPT-CL J0022-4144	5.55	-41.74	6.14	0.30	2.99×10^5	393.1	1.35×10^{16}	3.7
SPT-CL J0411-4819	62.82	-48.32	12.51	0.42	2.92×10^5	503.3	1.12×10^{16}	2.1
SPT-CL J0551-4339	87.88	-43.66	7.36	0.33	2.97×10^5	419.2	1.24×10^{16}	3.2
SPT-CL J2355-5055	358.95	-50.93	6.84	0.32	2.98×10^5	408.5	1.08×10^{16}	3.0
SPT-CL J0509-6118	77.47	-61.31	10.27	0.39	2.93×10^5	470.6	1.05×10^{16}	2.2
SPT-CL J0636-4942	99.17	-49.7	8.27	0.35	2.95×10^5	436.7	1.20×10^{16}	3.7
SPT-CL J0110-4445	17.59	-44.76	8.55	0.36	2.95×10^5	441.8	1.00×10^{16}	2.2
SPT-CL J0013-4906	3.33	-49.12	11.04	0.41	2.93×10^5	482.4	1.02×10^{16}	2.6
SPT-CL J0001-4842	0.28	-48.71	6.83	0.33	2.98×10^5	408.2	9.60×10^{15}	1.8
SPT-CL J0217-5245	34.3	-52.76	7.36	0.34	2.97×10^5	419.3	9.40×10^{15}	1.3
SPT-CL J0254-5857	43.57	-58.95	12.01	0.44	2.92×10^5	496.5	9.95×10^{15}	2.8
SPT-CL J2330-4502	352.57	-45.03	6.17	0.32	2.99×10^5	393.8	9.20×10^{15}	2.3
SPT-CL J0304-4401	46.07	-44.03	13.07	0.46	2.92×10^5	510.8	1.03×10^{16}	2.5
SPT-CL J0236-4938	39.25	-49.64	6.74	0.33	2.98×10^5	406.3	9.00×10^{15}	1.1

TABLE II – continued

SPT-CL J0600-4353	90.06	-43.89	7.79	0.36	2.96×10^5	427.7	9.06×10^{15}	2.0
SPT-CL J0052-5657	13.16	-56.96	5.95	0.32	2.99×10^5	388.9	8.80×10^{15}	0.8
SPT-CL J0650-4503	102.68	-45.06	9.61	0.40	2.94×10^5	459.9	9.18×10^{15}	2.1
SPT-CL J2059-5018	314.93	-50.31	6.16	0.33	2.99×10^5	393.7	8.70×10^{15}	2.6
SPT-CL J2131-4019	322.77	-40.32	11.66	0.45	2.92×10^5	491.4	9.20×10^{15}	0.6
SPT-CL J0416-6359	64.16	-64.0	6.83	0.35	2.98×10^5	408.2	8.50×10^{15}	2.0
SPT-CL J0424-4406	66.0	-44.11	7.24	0.36	2.97×10^5	416.8	8.52×10^{15}	1.4
SPT-CL J0240-5946	40.16	-59.77	8.92	0.4	2.95×10^5	448.3	8.60×10^{15}	2.5
SPT-CL J0144-4807	26.18	-48.13	5.84	0.33	2.99×10^5	386.2	8.10×10^{15}	1.0
SPT-CL J0405-4648	61.29	-46.81	7.2	0.36	2.97×10^5	416.0	8.25×10^{15}	1.2
SPT-CL J2358-6129	359.71	-61.49	6.79	0.36	2.98×10^5	407.5	8.10×10^{15}	2.0
SPT-CL J2135-5726	323.92	-57.44	9.77	0.43	2.93×10^5	462.7	8.60×10^{15}	3.5
SPT-CL J0330-5228	52.73	-52.47	10.48	0.44	2.93×10^5	473.8	8.50×10^{15}	1.2
SPT-CL J0412-5743	63.02	-57.72	6.06	0.34	2.99×10^5	391.4	7.94×10^{15}	1.7
SPT-CL J2332-5358	353.11	-53.97	8.54	0.40	2.95×10^5	441.6	8.20×10^{15}	1.4
SPT-CL J0012-5352	3.06	-53.87	5.95	0.34	2.99×10^5	388.8	7.85×10^{15}	2.0
SPT-CL J2205-5927	331.27	-59.46	6.66	0.37	2.98×10^5	404.6	7.60×10^{15}	0.5
SPT-CL J2344-4243	356.18	-42.72	18.1	0.6	2.92×10^5	569.1	9.36×10^{15}	1.6
SPT-CL J0402-4611	60.58	-46.19	6.2	0.36	2.99×10^5	394.6	7.35×10^{15}	2.0
SPT-CL J0052-4551	13.19	-45.86	6.2	0.36	2.99×10^5	394.4	7.33×10^{15}	2.0
SPT-CL J0243-4833	40.91	-48.56	12.1	0.5	2.92×10^5	497.7	8.12×10^{15}	1.0
SPT-CL J2022-6323	305.53	-63.4	6.99	0.38	2.99×10^5	411.6	7.50×10^{15}	3.2
SPT-CL J2327-5137	351.78	-51.62	5.39	0.34	3.01×10^5	375.2	7.25×10^{15}	2.5
SPT-CL J2316-5453	349.21	-54.9	6.48	0.37	2.98×10^5	400.8	7.26×10^{15}	1.6
SPT-CL J0344-5518	56.21	-55.3	5.94	0.36	3.00×10^5	388.5	7.10×10^{15}	2.0
SPT-CL J2145-5644	326.47	-56.75	10.87	0.48	2.93×10^5	479.8	7.90×10^{15}	2.8
SPT-CL J2223-5339	338.33	-53.65	9.0	0.44	2.94×10^5	449.6	7.40×10^{15}	1.0
SPT-CL J2159-6244	329.99	-62.74	6.96	0.39	2.97×10^5	411.0	7.10×10^{15}	1.7
SPT-CL J0445-4230	71.28	-42.51	7.77	0.41	2.96×10^5	427.2	7.16×10^{15}	2.0
SPT-CL J0551-5709	87.9	-57.16	8.13	0.42	2.96×10^5	434.1	7.15×10^{15}	0.7
SPT-CL J2124-6124	321.15	-61.41	8.45	0.44	2.94×10^5	439.9	7.25×10^{15}	2.8
SPT-CL J2351-5452	357.9	-54.88	6.5	0.38	2.98×10^5	401.2	6.80×10^{15}	0.5
SPT-CL J2206-4057	331.62	-40.95	5.63	0.36	3.00×10^5	381.1	6.70×10^{15}	1.2
SPT-CL J0252-4824	43.19	-48.41	7.76	0.42	2.96×10^5	427.0	6.90×10^{15}	0.0
SPT-CL J0429-4355	67.31	-43.93	5.85	0.37	2.99×10^5	386.3	6.60×10^{15}	0.8
SPT-CL J2259-5431	344.98	-54.53	6.47	0.39	2.98×10^5	400.5	6.63×10^{15}	1.2
SPT-CL J0025-5034	6.37	-50.57	5.88	0.38	3.00×10^5	387.0	6.40×10^{15}	0.3
SPT-CL J0447-5055	71.84	-50.92	6.57	0.4	2.98×10^5	402.7	6.47×10^{15}	0.2
SPT-CL J0019-4051	4.76	-40.86	9.61	0.48	2.93×10^5	459.9	6.86×10^{15}	1.0
SPT-CL J2136-4704	324.12	-47.08	7.35	0.43	2.96×10^5	419.1	6.45×10^{15}	0.5
SPT-CL J0354-5904	58.56	-59.07	7.02	0.42	2.97×10^5	412.2	6.35×10^{15}	1.4
SPT-CL J0333-5842	53.32	-58.7	5.47	0.37	3.01×10^5	377.3	6.15×10^{15}	0.4
SPT-CL J0244-4857	41.03	-48.96	6.76	0.41	2.97×10^5	406.9	6.24×10^{15}	0.3
SPT-CL J0342-4028	55.56	-40.48	7.59	0.44	2.96×10^5	423.7	6.40×10^{15}	1.9
SPT-CL J2030-5638	307.7	-56.64	6.07	0.39	2.99×10^5	391.5	6.10×10^{15}	0.5
SPT-CL J0509-5342	77.34	-53.71	8.27	0.46	2.95×10^5	436.6	6.34×10^{15}	0.2
SPT-CL J2319-4716	349.98	-47.28	6.98	0.43	2.97×10^5	411.5	6.10×10^{15}	1.8
SPT-CL J0611-5938	92.81	-59.64	5.75	0.39	3.00×10^5	384.1	5.90×10^{15}	0.3
SPT-CL J0054-4046	13.59	-40.78	6.3	0.41	2.99×10^5	396.7	6.00×10^{15}	1.3
SPT-CL J0505-4204	76.37	-42.08	5.94	0.4	3.00×10^5	388.6	5.90×10^{15}	2.0
SPT-CL J0655-5234	103.96	-52.57	8.39	0.47	2.92×10^5	438.9	6.25×10^{15}	1.0
SPT-CL J0334-4659	53.55	-46.99	8.95	0.49	2.94×10^5	448.5	6.34×10^{15}	1.6
SPT-CL J2016-4517	304.0	-45.3	5.9	0.4	3.00×10^5	387.6	5.90×10^{15}	1.1
SPT-CL J2342-4714	355.75	-47.24	5.82	0.4	3.00×10^5	385.6	5.84×10^{15}	1.6
SPT-CL J0047-4506	11.82	-45.11	8.11	0.47	2.95×10^5	433.7	6.15×10^{15}	1.4
SPT-CL J0439-5330	69.93	-53.5	6.22	0.41	2.98×10^5	394.9	5.80×10^{15}	0.0
SPT-CL J0647-5828	101.98	-58.48	7.14	0.44	2.97×10^5	414.7	6.10×10^{15}	1.8
SPT-CL J0341-5027	55.28	-50.46	5.48	0.39	3.01×10^5	377.3	5.66×10^{15}	0.5
SPT-CL J0254-6051	43.6	-60.86	7.09	0.44	2.97×10^5	413.7	5.88×10^{15}	1.0
SPT-CL J2140-5727	325.14	-57.46	5.92	0.40	3.00×10^5	387.9	5.70×10^{15}	0.1
SPT-CL J0452-4806	73.0	-48.11	5.29	0.38	3.01×10^5	372.7	5.65×10^{15}	0.5
SPT-CL J0259-4556	44.9	-45.94	6.58	0.43	2.98×10^5	402.8	5.75×10^{15}	1.1
SPT-CL J0626-4446	96.74	-44.77	6.92	0.44	2.97×10^5	410.2	5.80×10^{15}	0.2
SPT-CL J0237-4151	39.42	-41.86	5.78	0.41	3.00×10^5	384.7	5.55×10^{15}	0.0

TABLE II – continued

SPT-CL J2035-5251	308.8	-52.85	9.97	0.53	2.93×10^5	465.8	6.24×10^{15}	1.6
SPT-CL J0014-4036	3.74	-40.6	9.57	0.52	2.94×10^5	459.3	6.10×10^{15}	0.2
SPT-CL J0257-5842	44.39	-58.71	6.0	0.42	2.99×10^5	389.8	5.45×10^{15}	0.0
SPT-CL J0638-4243	99.57	-42.72	5.67	0.41	3.00×10^5	382.0	5.40×10^{15}	0.2
SPT-CL J0417-4748	64.35	-47.81	11.66	0.58	2.92×10^5	491.3	6.40×10^{15}	1.7
SPT-CL J0655-4429	103.76	-44.48	5.69	0.41	3.00×10^5	382.5	5.34×10^{15}	2.0
SPT-CL J0543-6219	85.76	-62.33	8.59	0.51	2.95×10^5	442.4	5.65×10^{15}	1.0
SPT-CL J2335-4544	353.79	-45.74	9.98	0.55	2.93×10^5	466.0	5.88×10^{15}	1.2
SPT-CL J2306-6505	346.73	-65.09	9.29	0.53	2.94×10^5	454.7	5.74×10^{15}	0.0
SPT-CL J0611-4724	92.92	-47.41	6.5	0.45	2.98×10^5	401.3	5.27×10^{15}	0.0
SPT-CL J2112-4434	318.21	-44.58	9.13	0.53	2.94×10^5	451.9	5.70×10^{15}	0.8
SPT-CL J0038-5244	9.72	-52.74	5.87	0.43	3.00×10^5	386.7	5.18×10^{15}	0.0
SPT-CL J2111-5339	317.92	-53.65	6.45	0.45	2.98×10^5	400.1	5.26×10^{15}	0.0
SPT-CL J0351-5636	57.93	-56.61	5.32	0.41	3.01×10^5	373.4	5.10×10^{15}	0.4
SPT-CL J0546-4752	86.55	-47.88	6.04	0.43	2.99×10^5	390.9	5.18×10^{15}	0.7
SPT-CL J2050-4213	312.57	-42.22	7.96	0.5	2.96×10^5	430.9	5.40×10^{15}	1.0
SPT-CL J0200-4852	30.14	-48.88	7.93	0.5	2.96×10^5	430.2	5.38×10^{15}	0.0
SPT-CL J0216-4830	34.07	-48.51	6.97	0.47	2.97×10^5	411.3	5.28×10^{15}	1.4
SPT-CL J0346-5439	56.72	-54.65	8.91	0.53	2.94×10^5	448.1	5.50×10^{15}	0.0
SPT-CL J2259-3952	344.81	-39.87	9.1	0.54	2.94×10^5	451.4	5.50×10^{15}	0.0
SPT-CL J0257-4817	44.45	-48.3	5.96	0.44	3.00×10^5	389.0	5.04×10^{15}	0.0
SPT-CL J0451-4952	72.97	-49.88	5.56	0.42	3.00×10^5	379.3	4.96×10^{15}	0.0
SPT-CL J0532-5450	83.03	-54.84	5.69	0.43	3.00×10^5	382.7	4.98×10^{15}	0.0
SPT-CL J0317-5935	49.32	-59.59	6.8	0.47	2.98×10^5	407.7	5.10×10^{15}	0.0
SPT-CL J0257-5732	44.35	-57.54	5.72	0.43	3.00×10^5	383.4	4.94×10^{15}	0.0
SPT-CL J2235-4416	338.86	-44.27	6.19	0.45	2.99×10^5	394.4	4.98×10^{15}	0.1
SPT-CL J0517-6311	79.41	-63.2	5.99	0.45	3.00×10^5	389.6	4.92×10^{15}	0.2
SPT-CL J0403-5719	60.97	-57.32	6.44	0.47	2.98×10^5	399.9	4.90×10^{15}	0.1
SPT-CL J0456-6141	74.15	-61.68	5.51	0.44	3.00×10^5	378.3	4.74×10^{15}	0.0
SPT-CL J0314-6130	48.61	-61.51	5.37	0.43	3.01×10^5	374.8	4.65×10^{15}	0.0
SPT-CL J0508-6149	77.16	-61.82	5.73	0.45	3.00×10^5	383.5	4.68×10^{15}	0.3
SPT-CL J0641-5950	100.38	-59.85	7.79	0.52	2.96×10^5	427.5	5.00×10^{15}	0.1
SPT-CL J0417-4427	64.41	-44.46	9.08	0.56	2.94×10^5	450.9	5.20×10^{15}	0.1
SPT-CL J0307-5042	46.95	-50.71	8.67	0.55	2.95×10^5	443.8	5.08×10^{15}	0.0
SPT-CL J0232-5257	38.19	-52.96	8.79	0.56	2.94×10^5	446.1	5.10×10^{15}	0.5
SPT-CL J0124-4301	21.15	-43.02	6.04	0.47	2.99×10^5	390.8	4.60×10^{15}	0.1
SPT-CL J2132-4349	323.17	-43.83	7.48	0.52	2.96×10^5	421.6	4.82×10^{15}	0.4
SPT-CL J2131-5003	322.97	-50.06	5.86	0.46	3.00×10^5	386.5	4.55×10^{15}	0.0
SPT-CL J0102-4915	15.73	-49.26	22.05	0.87	2.94×10^5	606.6	7.64×10^{15}	2.0
SPT-CL J0113-6105	18.4	-61.09	5.57	0.45	3.00×10^5	379.6	4.48×10^{15}	0.0
SPT-CL J0304-4748	46.15	-47.81	7.06	0.51	2.97×10^5	413.1	4.66×10^{15}	0.0
SPT-CL J2331-5051	352.96	-50.86	9.09	0.58	2.94×10^5	451.2	5.00×10^{15}	0.0
SPT-CL J0544-3950	86.25	-39.85	7.42	0.52	2.96×10^5	420.3	4.73×10^{15}	0.0
SPT-CL J0048-4548	12.25	-45.8	5.83	0.47	3.00×10^5	385.8	4.45×10^{15}	0.0
SPT-CL J0007-4706	1.75	-47.12	5.59	0.46	3.00×10^5	380.2	4.44×10^{15}	0.2
SPT-CL J0306-4749	46.74	-47.82	5.58	0.46	3.00×10^5	380.0	4.40×10^{15}	0.1
SPT-CL J0337-6300	54.47	-63.01	5.78	0.47	3.00×10^5	384.8	4.43×10^{15}	0.0
SPT-CL J0111-5424	17.77	-54.42	6.25	0.48	2.98×10^5	395.7	4.48×10^{15}	0.1
SPT-CL J0456-5116	74.12	-51.28	8.4	0.56	2.95×10^5	439.0	4.78×10^{15}	0.0
SPT-CL J0257-6050	44.34	-60.85	5.43	0.46	3.01×10^5	376.3	4.34×10^{15}	0.1
SPT-CL J0659-5300	104.78	-53.01	6.0	0.48	3.00×10^5	389.9	4.38×10^{15}	0.0
SPT-CL J2145-4348	326.36	-43.8	6.22	0.49	2.99×10^5	394.9	4.40×10^{15}	0.0
SPT-CL J0253-6046	43.46	-60.77	5.59	0.47	3.01×10^5	380.2	4.28×10^{15}	0.0
SPT-CL J2302-4435	345.59	-44.58	5.54	0.47	3.00×10^5	378.9	4.25×10^{15}	0.0
SPT-CL J2245-6206	341.26	-62.11	8.87	0.59	2.94×10^5	447.4	4.78×10^{15}	0.0
SPT-CL J0337-4928	54.46	-49.47	6.08	0.49	2.99×10^5	391.7	4.30×10^{15}	0.0
SPT-CL J2232-5959	338.15	-59.99	9.1	0.59	2.94×10^5	451.4	4.80×10^{15}	0.2
SPT-CL J2040-5342	310.22	-53.71	6.88	0.52	2.97×10^5	409.4	4.40×10^{15}	0.1
SPT-CL J0559-5249	89.93	-52.83	9.37	0.61	2.94×10^5	455.9	4.80×10^{15}	0.0
SPT-CL J0307-6225	46.83	-62.43	8.37	0.58	2.95×10^5	438.4	4.56×10^{15}	0.0
SPT-CL J0025-4133	6.49	-41.55	7.2	0.54	2.96×10^5	415.9	4.35×10^{15}	0.0
SPT-CL J0109-4045	17.48	-40.77	5.55	0.48	3.01×10^5	379.2	4.06×10^{15}	0.0
SPT-CL J0238-4904	39.7	-49.07	6.46	0.52	2.98×10^5	400.4	4.18×10^{15}	0.0
SPT-CL J0221-4446	35.42	-44.78	5.94	0.5	3.00×10^5	388.5	4.08×10^{15}	0.2

TABLE II – continued

SPT-CL J2051-6256	312.8	-62.93	5.54	0.48	3.01×10^5	378.9	4.00×10^{15}	0.1
SPT-CL J0218-4315	34.58	-43.26	9.43	0.63	2.94×10^5	456.9	4.63×10^{15}	0.1
SPT-CL J0106-5355	16.57	-53.93	5.82	0.5	3.00×10^5	385.7	4.00×10^{15}	0.0
SPT-CL J0219-4934	34.81	-49.58	7.01	0.55	2.97×10^5	412.0	4.19×10^{15}	0.0
SPT-CL J0111-5518	17.84	-55.31	5.44	0.49	3.01×10^5	376.6	3.96×10^{15}	0.0
SPT-CL J0351-4109	57.75	-41.16	8.92	0.62	2.94×10^5	448.3	4.50×10^{15}	0.1
SPT-CL J2017-6258	304.48	-62.98	6.62	0.54	2.98×10^5	403.8	4.10×10^{15}	0.3
SPT-CL J2148-6116	327.18	-61.28	7.5	0.57	2.96×10^5	422.0	4.20×10^{15}	0.0
SPT-CL J0619-5802	94.92	-58.04	7.0	0.55	2.97×10^5	411.9	4.12×10^{15}	0.2
SPT-CL J0135-5902	23.79	-59.04	5.85	0.51	3.00×10^5	386.4	3.90×10^{15}	0.1
SPT-CL J0041-5107	10.29	-51.13	5.57	0.5	3.00×10^5	379.8	3.85×10^{15}	0.0
SPT-CL J0342-5354	55.52	-53.91	6.02	0.52	2.99×10^5	390.3	3.90×10^{15}	0.0
SPT-CL J0135-5904	23.98	-59.08	5.41	0.5	3.01×10^5	375.8	3.78×10^{15}	0.1
SPT-CL J0343-5518	55.76	-55.3	6.48	0.54	2.98×10^5	400.8	3.94×10^{15}	0.0
SPT-CL J0033-6326	8.48	-63.45	7.93	0.6	2.96×10^5	430.3	4.17×10^{15}	0.1
SPT-CL J0212-4657	33.11	-46.95	9.55	0.65	2.94×10^5	459.0	4.45×10^{15}	0.2
SPT-CL J0410-6343	62.52	-63.73	6.11	0.53	2.99×10^5	392.5	3.82×10^{15}	0.0
SPT-CL J0336-4005	54.16	-40.1	5.8	0.52	3.00×10^5	385.2	3.75×10^{15}	0.2
SPT-CL J0217-4310	34.41	-43.18	7.07	0.57	2.97×10^5	413.3	3.96×10^{15}	0.0
SPT-CL J2218-4519	334.75	-45.32	8.8	0.64	2.94×10^5	446.1	4.26×10^{15}	0.1
SPT-CL J0429-5233	67.43	-52.56	5.21	0.5	3.02×10^5	370.6	3.66×10^{15}	0.0
SPT-CL J2337-5942	354.35	-59.7	13.26	0.78	2.92×10^5	513.2	5.10×10^{15}	0.3
SPT-CL J2155-6048	328.99	-60.81	6.11	0.54	2.99×10^5	392.3	3.74×10^{15}	0.0
SPT-CL J2350-5301	357.73	-53.02	6.11	0.54	2.99×10^5	392.4	3.72×10^{15}	0.0
SPT-CL J0542-4100	85.72	-41.0	8.61	0.64	2.94×10^5	442.8	4.15×10^{15}	0.0
SPT-CL J2222-4834	335.71	-48.57	8.95	0.65	2.94×10^5	448.8	4.20×10^{15}	0.0
SPT-CL J0522-5026	80.52	-50.44	5.55	0.52	3.00×10^5	379.2	3.62×10^{15}	0.3
SPT-CL J0309-4958	47.26	-49.97	6.32	0.55	2.99×10^5	397.3	3.72×10^{15}	0.0
SPT-CL J0202-5401	30.58	-54.02	6.31	0.55	2.99×10^5	397.1	3.70×10^{15}	0.0
SPT-CL J0426-5455	66.52	-54.92	8.53	0.64	2.95×10^5	441.4	4.08×10^{15}	0.1
SPT-CL J0142-5032	25.55	-50.54	9.55	0.68	2.94×10^5	458.9	4.30×10^{15}	0.4
SPT-CL J0402-6130	60.71	-61.5	5.41	0.52	3.01×10^5	375.8	3.54×10^{15}	0.0
SPT-CL J0011-4614	2.98	-46.24	6.0	0.54	2.99×10^5	389.8	3.66×10^{15}	0.3
SPT-CL J2155-5224	328.89	-52.41	6.11	0.55	2.99×10^5	392.5	3.68×10^{15}	0.2
SPT-CL J0444-4352	71.17	-43.87	5.7	0.53	3.00×10^5	383.0	3.58×10^{15}	0.1
SPT-CL J2020-6314	305.03	-63.24	5.78	0.54	3.00×10^5	384.8	3.56×10^{15}	0.1
SPT-CL J0030-5213	7.53	-52.22	5.58	0.53	3.00×10^5	379.9	3.54×10^{15}	0.1
SPT-CL J0512-5139	78.16	-51.66	6.38	0.57	2.98×10^5	398.6	3.66×10^{15}	0.3
SPT-CL J0152-5303	28.23	-53.05	7.34	0.61	2.97×10^5	418.8	3.77×10^{15}	0.0
SPT-CL J2206-5807	331.66	-58.13	7.02	0.6	2.97×10^5	412.3	3.72×10^{15}	0.0
SPT-CL J0157-4007	29.45	-40.13	6.4	0.57	2.99×10^5	398.9	3.60×10^{15}	0.1
SPT-CL J0649-4510	102.45	-45.17	5.96	0.55	3.00×10^5	389.0	3.52×10^{15}	0.2
SPT-CL J0543-4250	85.94	-42.84	7.58	0.62	2.96×10^5	423.6	3.77×10^{15}	0.0
SPT-CL J2110-5244	317.55	-52.75	7.12	0.61	2.97×10^5	414.4	3.65×10^{15}	0.0
SPT-CL J0243-5930	40.86	-59.51	7.7	0.64	2.96×10^5	426.0	3.75×10^{15}	0.0
SPT-CL J0217-5014	34.27	-50.24	5.43	0.54	3.01×10^5	376.2	3.36×10^{15}	0.0
SPT-CL J0256-5617	44.1	-56.3	7.55	0.64	2.96×10^5	423.0	3.68×10^{15}	0.0
SPT-CL J2312-4621	348.06	-46.35	7.31	0.63	2.97×10^5	418.3	3.63×10^{15}	0.0
SPT-CL J2354-5633	358.71	-56.55	5.78	0.56	3.00×10^5	384.9	3.35×10^{15}	0.0
SPT-CL J2220-4534	335.08	-45.58	7.47	0.64	2.96×10^5	421.4	3.60×10^{15}	0.2
SPT-CL J0519-4248	79.85	-42.81	5.75	0.57	3.00×10^5	383.9	3.30×10^{15}	0.0
SPT-CL J0422-5140	65.59	-51.68	6.22	0.59	2.99×10^5	395.1	3.38×10^{15}	0.1
SPT-CL J2140-5331	325.03	-53.52	5.67	0.57	3.00×10^5	382.2	3.25×10^{15}	0.1
SPT-CL J2146-5736	326.7	-57.61	6.42	0.60	2.98×10^5	399.5	3.40×10^{15}	0.5
SPT-CL J0334-4815	53.71	-48.26	7.3	0.64	2.97×10^5	417.9	3.55×10^{15}	0.2
SPT-CL J0148-4518	27.1	-45.3	5.78	0.57	3.00×10^5	384.8	3.25×10^{15}	0.1
SPT-CL J2146-4846	326.53	-48.78	6.79	0.62	2.98×10^5	407.5	3.20×10^{15}	0.3
SPT-CL J0123-4821	20.79	-48.36	7.53	0.66	2.96×10^5	422.5	3.55×10^{15}	0.1
SPT-CL J0145-4426	26.28	-44.44	5.53	0.57	3.00×10^5	378.6	2.84×10^{15}	0.2
SPT-CL J2317-4707	349.27	-47.12	5.49	0.57	3.01×10^5	377.9	2.80×10^{15}	0.0
SPT-CL J0352-5647	58.24	-56.8	7.28	0.65	2.96×10^5	417.6	3.48×10^{15}	0.1
SPT-CL J0231-5403	37.78	-54.06	5.85	0.59	3.00×10^5	386.4	3.20×10^{15}	0.0
SPT-CL J0231-4427	37.75	-44.46	6.0	0.6	3.00×10^5	389.9	3.18×10^{15}	0.0
SPT-CL J2109-5040	317.38	-50.68	6.39	0.62	2.99×10^5	398.7	3.25×10^{15}	0.0

TABLE II – continued

SPT-CL J0615-5746	93.96	-57.78	5.82	0.97	2.92×10^5	552.8	5.32×10^{15}	0.0
SPT-CL J0511-5154	77.92	-51.9	6.98	0.65	2.97×10^5	411.5	3.14×10^{15}	0.1
SPT-CL J0307-4123	46.88	-41.39	5.82	0.59	3.00×10^5	385.6	2.82×10^{15}	0.1
SPT-CL J0216-4219	34.06	-42.33	6.34	0.62	2.99×10^5	397.7	3.22×10^{15}	0.0
SPT-CL J0612-4317	93.02	-43.3	6.74	0.64	2.98×10^5	406.4	3.26×10^{15}	0.0
SPT-CL J2118-5055	319.73	-50.93	6.37	0.63	2.98×10^5	398.3	3.18×10^{15}	0.0
SPT-CL J0622-4645	95.71	-46.77	5.88	0.60	3.00×10^5	387.1	2.79×10^{15}	0.0
SPT-CL J0341-6143	55.35	-61.72	6.07	0.61	2.99×10^5	391.6	3.12×10^{15}	0.0
SPT-CL J0049-5315	12.38	-53.25	7.01	0.66	2.97×10^5	412.1	3.25×10^{15}	0.0
SPT-CL J0000-5748	0.25	-57.81	7.68	0.70	2.96×10^5	425.5	3.40×10^{15}	0.0
SPT-CL J0014-4952	3.7	-49.88	8.86	0.75	2.94×10^5	447.3	3.54×10^{15}	0.0
SPT-CL J0521-5104	80.3	-51.08	7.04	0.68	2.97×10^5	412.7	3.19×10^{15}	0.0
SPT-CL J0233-5819	38.26	-58.33	6.78	0.66	2.98×10^5	407.2	3.14×10^{15}	0.0
SPT-CL J2134-4109	323.53	-41.16	7.3	0.7	2.97×10^5	418.0	3.20×10^{15}	0.0
SPT-CL J0359-5218	59.84	-52.32	6.49	0.66	2.98×10^5	401.0	3.04×10^{15}	0.0
SPT-CL J0528-4417	82.06	-44.29	6.01	0.64	2.99×10^5	370.2	2.34×10^{15}	0.6
SPT-CL J0021-4902	5.38	-49.04	6.04	0.64	2.99×10^5	390.8	2.67×10^{15}	0.0
SPT-CL J0310-4647	47.63	-46.78	7.4	0.71	2.96×10^5	419.9	3.18×10^{15}	0.0
SPT-CL J2043-5035	310.83	-50.59	7.74	0.72	2.96×10^5	426.7	3.20×10^{15}	0.0
SPT-CL J0324-6236	51.05	-62.6	8.29	0.75	2.95×10^5	437.1	3.33×10^{15}	0.0
SPT-CL J0441-4855	70.45	-48.92	8.09	0.74	2.96×10^5	433.3	3.24×10^{15}	0.0
SPT-CL J0406-4805	61.73	-48.09	7.81	0.74	2.93×10^5	428.0	3.25×10^{15}	0.0
SPT-CL J2358-4354	359.73	-43.90	6.29	0.67	2.99×10^5	396.6	2.64×10^{15}	0.0
SPT-CL J0230-6028	37.64	-60.47	6.29	0.67	2.98×10^5	396.6	2.64×10^{15}	0.0
SPT-CL J2259-6057	344.75	-60.95	9.16	0.81	2.94×10^5	452.4	3.42×10^{15}	0.0
SPT-CL J2034-5936	308.54	-59.6	7.96	0.76	2.95×10^5	430.8	3.20×10^{15}	0.0
SPT-CL J0103-4250	15.91	-42.83	6.95	0.71	2.97×10^5	410.7	2.98×10^{15}	0.0
SPT-CL J0118-5156	19.60	-51.94	6.58	0.70	2.98×10^5	402.9	2.64×10^{15}	0.1
SPT-CL J0449-4901	72.27	-49.02	8.25	0.79	2.95×10^5	436.3	3.18×10^{15}	0.0
SPT-CL J2106-4421	316.57	-44.35	7.81	0.78	2.96×10^5	427.9	3.02×10^{15}	0.0
SPT-CL J0131-5604	22.93	-56.08	6.95	0.75	2.97×10^5	373.1	2.02×10^{15}	0.1
SPT-CL J0641-4733	100.29	-47.57	7.40	0.78	2.97×10^5	419.9	2.64×10^{15}	0.0
SPT-CL J2258-4044	344.71	-40.74	9.65	0.90	2.94×10^5	460.6	3.34×10^{15}	0.0
SPT-CL J2301-4023	345.47	-40.39	7.93	0.83	2.96×10^5	430.4	2.68×10^{15}	0.0
SPT-CL J0058-6145	14.58	-61.76	7.59	0.69	2.96×10^5	423.7	3.04×10^{15}	0.1
SPT-CL J2146-4633	326.65	-46.55	9.17	0.93	2.94×10^5	452.6	3.07×10^{15}	0.0
SPT-CL J0646-6236	101.64	-62.61	8.26	0.89	2.95×10^5	436.5	2.45×10^{15}	0.0
SPT-CL J2106-5844	316.52	-58.75	13.57	1.13	2.95×10^5	517.3	4.04×10^{15}	0.0
SPT-CL J2341-5119	355.30	-51.33	9.36	1.00	2.94×10^5	455.8	2.78×10^{15}	0.0

VI. UPPER LIMITS ON ANNIHILATION CROSS-SECTION FOR ALL CLUSTERS

We now calculate the calculate upper limits on the annihilation cross-section for $b\bar{b}$ and $\tau^+\tau^-$ annihilation channels for all the 350 clusters in our sample. These limits are collated in Table III. Amongst all the remaining clusters, we found the most stringent limit for SPT-CL J0455-4159, viz. $\langle\sigma v\rangle = 6.44 \times 10^{-26} \text{ cm}^3 \text{s}^{-1}$ for $m_\chi = 10 \text{ GeV}$ and $b\bar{b}$ annihilation channel. The corresponding limit for $\tau^+\tau^-$ annihilation channel for this cluster is given by $\langle\sigma v\rangle = 8.26 \times 10^{-26} \text{ cm}^3 \text{s}^{-1}$ for $m_\chi = 10 \text{ GeV}$.

TABLE III: 95% c.l. upper limits on $\langle\sigma v\rangle$ for all 350 clusters for $b\bar{b}$ and $\tau^+\tau^-$ annihilation channels for WIMP mass of 10 GeV.

Cluster Name	$b\bar{b} (\text{cm}^3 \text{s}^{-1})$	$\tau^+\tau^- (\text{cm}^3 \text{s}^{-1})$
SPT-CL J2012-5649	6.95×10^{-25}	9.44×10^{-25}
SPT-CL J0431-6126	6.20×10^{-25}	8.10×10^{-25}
SPT-CL J2313-4243	5.97×10^{-25}	6.72×10^{-25}
SPT-CL J2009-4518	5.93×10^{-25}	8.14×10^{-25}
SPT-CL J2201-5956	3.14×10^{-25}	7.72×10^{-25}

TABLE III – continued

SPT-CL J0328-5541	1.75×10^{-25}	6.54×10^{-25}
SPT-CL J2217-6509	4.28×10^{-25}	6.44×10^{-25}
SPT-CL J2249-6426	3.08×10^{-25}	6.92×10^{-25}
SPT-CL J0145-5301	7.52×10^{-25}	7.60×10^{-25}
SPT-CL J0645-5413	5.74×10^{-25}	8.90×10^{-25}
SPT-CL J0500-5116	1.15×10^{-25}	7.15×10^{-25}
SPT-CL J2055-5456	6.50×10^{-25}	8.96×10^{-25}
SPT-CL J0628-4143	4.10×10^{-25}	6.82×10^{-25}
SPT-CL J0404-6510	1.92×10^{-25}	7.34×10^{-25}
SPT-CL J0641-5001	1.23×10^{-25}	7.72×10^{-25}
SPT-CL J0411-6340	2.21×10^{-25}	6.84×10^{-25}
SPT-CL J0145-6033	6.80×10^{-25}	6.52×10^{-25}
SPT-CL J2021-5257	9.95×10^{-26}	1.80×10^{-25}
SPT-CL J0638-5358	2.37×10^{-25}	5.24×10^{-25}
SPT-CL J2012-4130	2.12×10^{-25}	4.64×10^{-25}
SPT-CL J0516-6312	1.80×10^{-25}	4.10×10^{-25}
SPT-CL J2259-5617	2.42×10^{-25}	4.60×10^{-25}
SPT-CL J0027-5015	1.90×10^{-25}	4.64×10^{-25}
SPT-CL J0525-4715	2.00×10^{-25}	5.43×10^{-25}
SPT-CL J2254-5805	1.35×10^{-25}	5.25×10^{-25}
SPT-CL J0537-6504	2.50×10^{-25}	5.75×10^{-25}
SPT-CL J0658-5556	1.65×10^{-25}	4.95×10^{-25}
SPT-CL J0510-4519	2.15×10^{-25}	4.25×10^{-25}
SPT-CL J0637-4829	1.05×10^{-25}	5.44×10^{-25}
SPT-CL J2134-4238	2.55×10^{-25}	5.50×10^{-25}
SPT-CL J0051-4834	1.15×10^{-25}	5.10×10^{-25}
SPT-CL J0317-4849	2.32×10^{-25}	5.52×10^{-25}
SPT-CL J2023-5535	1.85×10^{-25}	5.00×10^{-25}
SPT-CL J0232-4421	2.65×10^{-25}	5.02×10^{-25}
SPT-CL J0216-4816	1.55×10^{-25}	4.84×10^{-25}
SPT-CL J2025-5117	2.22×10^{-25}	4.02×10^{-25}
SPT-CL J0010-5112	1.75×10^{-25}	4.20×10^{-25}
SPT-CL J2254-6314	2.50×10^{-25}	4.04×10^{-25}
SPT-CL J2248-4431	1.25×10^{-25}	5.24×10^{-25}
SPT-CL J0013-4621	2.35×10^{-25}	4.62×10^{-25}
SPT-CL J2020-4646	1.75×10^{-25}	5.00×10^{-25}
SPT-CL J0504-4929	2.60×10^{-25}	5.80×10^{-25}
SPT-CL J0225-4155	1.40×10^{-25}	4.44×10^{-25}
SPT-CL J0458-5741	2.35×10^{-25}	4.80×10^{-25}
SPT-CL J2241-4236	1.60×10^{-25}	5.50×10^{-25}
SPT-CL J0108-4341	2.55×10^{-25}	6.96×10^{-25}
SPT-CL J0124-5937	2.76×10^{-25}	4.95×10^{-25}
SPT-CL J0256-4736	3.08×10^{-25}	4.10×10^{-25}
SPT-CL J0653-5744	2.42×10^{-25}	2.44×10^{-25}
SPT-CL J2211-4833	2.15×10^{-25}	5.65×10^{-25}
SPT-CL J0118-5638	1.90×10^{-25}	3.90×10^{-25}
SPT-CL J0651-4037	2.63×10^{-25}	2.75×10^{-25}
SPT-CL J2121-6335	2.34×10^{-25}	6.20×10^{-25}
SPT-CL J0001-6258	1.80×10^{-25}	4.52×10^{-25}
SPT-CL J0235-5121	2.50×10^{-25}	2.10×10^{-25}
SPT-CL J2005-5635	1.55×10^{-25}	5.85×10^{-25}
SPT-CL J2254-4620	2.24×10^{-25}	3.43×10^{-25}
SPT-CL J0549-6205	1.46×10^{-25}	2.90×10^{-25}
SPT-CL J0516-5430	8.72×10^{-26}	2.75×10^{-25}
SPT-CL J2031-4037	1.20×10^{-25}	4.20×10^{-25}
SPT-CL J0225-4327	2.11×10^{-25}	2.60×10^{-25}
SPT-CL J0040-4407	1.00×10^{-25}	5.05×10^{-25}
SPT-CL J0620-4715	2.63×10^{-25}	3.74×10^{-25}
SPT-CL J2019-5642	1.78×10^{-25}	2.22×10^{-25}
SPT-CL J0249-5658	2.33×10^{-25}	6.31×10^{-25}
SPT-CL J0603-4714	1.56×10^{-25}	4.95×10^{-25}
SPT-CL J0601-4122	2.27×10^{-25}	2.42×10^{-25}
SPT-CL J2138-6008	1.24×10^{-25}	5.65×10^{-25}
SPT-CL J2032-5627	2.40×10^{-25}	3.55×10^{-25}

TABLE III – continued

SPT-CL J2223-5015	1.01×10^{-25}	2.20×10^{-25}
SPT-CL J0412-5106	2.12×10^{-25}	6.40×10^{-25}
SPT-CL J2120-4016	1.30×10^{-25}	4.66×10^{-25}
SPT-CL J2219-5708	1.14×10^{-25}	2.95×10^{-25}
SPT-CL J2300-5331	8.85×10^{-26}	1.00×10^{-25}
SPT-CL J2027-4240	1.25×10^{-25}	4.10×10^{-25}
SPT-CL J0555-6406	1.04×10^{-25}	3.44×10^{-25}
SPT-CL J0311-6354	1.36×10^{-25}	5.66×10^{-25}
SPT-CL J0129-6432	1.00×10^{-25}	2.85×10^{-25}
SPT-CL J0505-6145	1.64×10^{-25}	3.74×10^{-25}
SPT-CL J0133-6434	1.27×10^{-25}	5.20×10^{-25}
SPT-CL J2325-4111	1.85×10^{-25}	2.32×10^{-25}
SPT-CL J0438-5419	9.45×10^{-26}	1.54×10^{-25}
SPT-CL J0405-4916	1.32×10^{-25}	3.10×10^{-25}
SPT-CL J2344-4224	1.70×10^{-25}	5.86×10^{-25}
SPT-CL J0150-4511	1.03×10^{-25}	2.63×10^{-25}
SPT-CL J0041-4428	1.44×10^{-25}	4.40×10^{-25}
SPT-CL J0214-4638	1.55×10^{-25}	3.95×10^{-25}
SPT-CL J0143-4452	9.82×10^{-26}	3.00×10^{-25}
SPT-CL J0655-5541	1.34×10^{-25}	2.14×10^{-25}
SPT-CL J2101-5542	1.07×10^{-25}	4.76×10^{-25}
SPT-CL J0440-4657	1.75×10^{-25}	3.24×10^{-25}
SPT-CL J0106-5943	1.23×10^{-25}	5.12×10^{-25}
SPT-CL J2130-6458	1.84×10^{-25}	2.88×10^{-25}
SPT-CL J0439-4600	1.00×10^{-25}	4.32×10^{-25}
SPT-CL J2011-5725	1.36×10^{-25}	3.55×10^{-25}
SPT-CL J0348-4515	1.64×10^{-25}	5.73×10^{-25}
SPT-CL J0304-4921	1.17×10^{-25}	2.42×10^{-25}
SPT-CL J0455-4159	6.44×10^{-26}	8.26×10^{-26}
SPT-CL J2223-5227	1.72×10^{-25}	3.80×10^{-25}
SPT-CL J2115-4659	1.00×10^{-25}	5.10×10^{-25}
SPT-CL J2016-4954	1.32×10^{-25}	2.10×10^{-25}
SPT-CL J0522-4818	6.38×10^{-25}	4.05×10^{-25}
SPT-CL J0151-5654	4.83×10^{-25}	3.20×10^{-25}
SPT-CL J0234-5831	7.25×10^{-25}	5.35×10^{-25}
SPT-CL J0114-4123	5.66×10^{-25}	2.73×10^{-25}
SPT-CL J0022-4144	9.35×10^{-26}	1.25×10^{-25}
SPT-CL J0411-4819	6.90×10^{-25}	3.90×10^{-25}
SPT-CL J0551-4339	5.35×10^{-25}	5.55×10^{-25}
SPT-CL J2355-5055	7.52×10^{-25}	2.55×10^{-25}
SPT-CL J0509-6118	5.00×10^{-25}	4.12×10^{-25}
SPT-CL J0636-4942	9.35×10^{-26}	1.60×10^{-25}
SPT-CL J0110-4445	5.65×10^{-25}	5.74×10^{-25}
SPT-CL J0013-4906	4.20×10^{-25}	2.30×10^{-25}
SPT-CL J0001-4842	6.40×10^{-25}	4.82×10^{-25}
SPT-CL J0217-5245	7.00×10^{-25}	3.14×10^{-25}
SPT-CL J0254-5857	5.74×10^{-25}	5.00×10^{-25}
SPT-CL J2330-4502	4.82×10^{-25}	2.84×10^{-25}
SPT-CL J0304-4401	6.64×10^{-25}	4.70×10^{-25}
SPT-CL J0236-4938	5.20×10^{-25}	3.35×10^{-25}
SPT-CL J0600-4353	7.40×10^{-25}	5.22×10^{-25}
SPT-CL J0052-5657	4.54×10^{-25}	2.15×10^{-25}
SPT-CL J0650-4503	6.72×10^{-25}	4.60×10^{-25}
SPT-CL J2059-5018	5.82×10^{-25}	3.85×10^{-25}
SPT-CL J2131-4019	4.10×10^{-25}	5.10×10^{-25}
SPT-CL J0416-6359	7.10×10^{-25}	1.10×10^{-24}
SPT-CL J0424-4406	5.00×10^{-25}	8.43×10^{-25}
SPT-CL J0240-5946	6.30×10^{-25}	1.66×10^{-24}
SPT-CL J0144-4807	4.80×10^{-25}	7.88×10^{-25}
SPT-CL J0405-4648	7.70×10^{-25}	1.32×10^{-24}
SPT-CL J2358-6129	5.62×10^{-25}	6.54×10^{-25}
SPT-CL J2135-5726	9.85×10^{-26}	1.84×10^{-25}
SPT-CL J0330-5228	6.50×10^{-25}	9.22×10^{-25}
SPT-CL J0412-5743	5.20×10^{-25}	1.46×10^{-24}

TABLE III – continued

SPT-CL J2332-5358	7.30×10^{-25}	7.80×10^{-25}
SPT-CL J0012-5352	4.73×10^{-25}	1.00×10^{-24}
SPT-CL J2205-5927	6.20×10^{-25}	1.42×10^{-24}
SPT-CL J2344-4243	5.45×10^{-25}	8.14×10^{-25}
SPT-CL J0402-4611	4.90×10^{-25}	1.70×10^{-24}
SPT-CL J0052-4551	7.00×10^{-25}	6.86×10^{-25}
SPT-CL J0243-4833	5.80×10^{-25}	1.35×10^{-24}
SPT-CL J2022-6323	4.30×10^{-25}	9.54×10^{-25}
SPT-CL J2327-5137	6.10×10^{-25}	1.24×10^{-24}
SPT-CL J2316-5453	5.63×10^{-25}	1.90×10^{-24}
SPT-CL J0344-5518	4.60×10^{-25}	7.44×10^{-25}
SPT-CL J2145-5644	7.28×10^{-25}	1.80×10^{-24}
SPT-CL J2233-5339	5.10×10^{-25}	6.35×10^{-25}
SPT-CL J2159-6244	6.70×10^{-25}	1.66×10^{-24}
SPT-CL J0445-4230	4.32×10^{-25}	9.00×10^{-25}
SPT-CL J0551-5709	7.90×10^{-25}	1.52×10^{-24}
SPT-CL J2124-6124	5.90×10^{-25}	7.24×10^{-25}
SPT-CL J2351-5452	6.32×10^{-25}	1.76×10^{-24}
SPT-CL J2206-4057	1.05×10^{-24}	1.74×10^{-24}
SPT-CL J0252-4824	1.56×10^{-24}	6.38×10^{-25}
SPT-CL J0429-4355	1.25×10^{-24}	1.00×10^{-24}
SPT-CL J2259-5431	1.80×10^{-24}	1.82×10^{-24}
SPT-CL J0025-5034	1.10×10^{-24}	8.82×10^{-25}
SPT-CL J0447-5055	1.70×10^{-24}	1.46×10^{-24}
SPT-CL J0019-4051	1.90×10^{-24}	7.16×10^{-25}
SPT-CL J2136-4704	1.45×10^{-24}	1.94×10^{-24}
SPT-CL J0354-5904	1.40×10^{-24}	6.92×10^{-25}
SPT-CL J0333-5842	1.80×10^{-24}	1.56×10^{-24}
SPT-CL J0244-4857	1.10×10^{-24}	9.34×10^{-25}
SPT-CL J0342-4028	1.90×10^{-24}	1.86×10^{-24}
SPT-CL J2030-5638	1.02×10^{-24}	7.24×10^{-25}
SPT-CL J0509-5342	1.70×10^{-24}	1.00×10^{-24}
SPT-CL J2319-4716	1.54×10^{-24}	1.56×10^{-24}
SPT-CL J0611-5938	1.16×10^{-24}	1.70×10^{-24}
SPT-CL J0054-4046	1.72×10^{-24}	6.44×10^{-25}
SPT-CL J0505-4204	1.30×10^{-24}	1.20×10^{-24}
SPT-CL J0655-5234	1.40×10^{-24}	1.84×10^{-24}
SPT-CL J0334-4659	1.20×10^{-24}	8.10×10^{-25}
SPT-CL J2016-4517	1.10×10^{-24}	1.74×10^{-24}
SPT-CL J2342-4714	1.65×10^{-24}	7.70×10^{-25}
SPT-CL J0047-4506	1.20×10^{-24}	1.66×10^{-24}
SPT-CL J0439-5330	1.48×10^{-24}	5.64×10^{-24}
SPT-CL J0647-5828	1.58×10^{-24}	3.52×10^{-24}
SPT-CL J0341-5027	1.88×10^{-24}	6.20×10^{-24}
SPT-CL J0254-6051	1.30×10^{-24}	4.82×10^{-24}
SPT-CL J2140-5727	1.45×10^{-24}	5.30×10^{-24}
SPT-CL J0452-4806	1.22×10^{-24}	3.26×10^{-24}
SPT-CL J0259-4556	1.83×10^{-24}	6.50×10^{-24}
SPT-CL J0626-4446	1.15×10^{-24}	4.00×10^{-24}
SPT-CL J0237-4151	2.00×10^{-24}	5.84×10^{-24}
SPT-CL J2035-5251	1.74×10^{-24}	3.70×10^{-24}
SPT-CL J0014-4036	1.12×10^{-24}	6.40×10^{-24}
SPT-CL J0257-5842	1.45×10^{-24}	4.65×10^{-24}
SPT-CL J0638-4243	1.60×10^{-24}	5.12×10^{-24}
SPT-CL J0417-4748	1.45×10^{-24}	3.94×10^{-24}
SPT-CL J0655-4429	1.20×10^{-24}	6.72×10^{-24}
SPT-CL J0543-6219	1.92×10^{-24}	4.24×10^{-24}
SPT-CL J2335-4544	1.30×10^{-24}	5.75×10^{-24}
SPT-CL J2306-6505	1.90×10^{-24}	3.80×10^{-24}
SPT-CL J0611-4724	1.70×10^{-24}	6.07×10^{-24}
SPT-CL J2112-4434	1.35×10^{-24}	4.10×10^{-24}
SPT-CL J0038-5244	1.60×10^{-24}	5.95×10^{-24}
SPT-CL J2111-5339	1.26×10^{-24}	3.65×10^{-24}
SPT-CL J0351-5636	1.44×10^{-24}	6.90×10^{-24}

TABLE III – continued

SPT-CL J0546-4752	1.80×10^{-24}	4.45×10^{-24}
SPT-CL J2050-4213	1.55×10^{-24}	5.38×10^{-24}
SPT-CL J0200-4852	1.64×10^{-24}	7.14×10^{-24}
SPT-CL J0216-4830	1.70×10^{-24}	8.46×10^{-24}
SPT-CL J0346-5439	1.06×10^{-24}	6.74×10^{-24}
SPT-CL J2259-3952	1.75×10^{-24}	8.20×10^{-24}
SPT-CL J0257-4817	1.18×10^{-24}	7.88×10^{-24}
SPT-CL J0451-4952	1.30×10^{-24}	6.55×10^{-24}
SPT-CL J0532-5450	9.85×10^{-25}	8.65×10^{-24}
SPT-CL J0317-5935	1.68×10^{-24}	7.36×10^{-24}
SPT-CL J0257-5732	1.04×10^{-24}	7.00×10^{-24}
SPT-CL J2235-4416	1.50×10^{-24}	8.82×10^{-24}
SPT-CL J0517-6311	8.75×10^{-25}	7.00×10^{-24}
SPT-CL J0403-5719	1.42×10^{-24}	6.45×10^{-24}
SPT-CL J0456-6141	1.25×10^{-24}	8.18×10^{-24}
SPT-CL J0314-6130	1.90×10^{-24}	7.74×10^{-24}
SPT-CL J0508-6149	1.10×10^{-24}	6.86×10^{-24}
SPT-CL J0641-5950	1.54×10^{-24}	8.40×10^{-24}
SPT-CL J0417-4427	1.34×10^{-24}	7.55×10^{-24}
SPT-CL J0307-5042	1.72×10^{-24}	6.24×10^{-24}
SPT-CL J0232-5257	1.05×10^{-24}	8.90×10^{-24}
SPT-CL J0124-4301	1.10×10^{-24}	7.45×10^{-24}
SPT-CL J2132-4349	1.64×10^{-24}	6.80×10^{-24}
SPT-CL J2131-5003	9.42×10^{-25}	8.35×10^{-24}
SPT-CL J0102-4915	1.20×10^{-24}	7.70×10^{-24}
SPT-CL J0113-6105	1.40×10^{-24}	6.10×10^{-24}
SPT-CL J0304-4748	1.60×10^{-24}	8.53×10^{-24}
SPT-CL J2331-5051	8.30×10^{-25}	7.25×10^{-24}
SPT-CL J0544-3950	1.32×10^{-24}	6.74×10^{-24}
SPT-CL J0048-4548	1.08×10^{-24}	8.76×10^{-24}
SPT-CL J0007-4706	1.82×10^{-24}	7.90×10^{-24}
SPT-CL J0306-4749	1.00×10^{-24}	6.40×10^{-24}
SPT-CL J0337-6300	1.36×10^{-24}	8.00×10^{-24}
SPT-CL J0111-5424	1.55×10^{-24}	7.82×10^{-24}
SPT-CL J0456-5116	1.67×10^{-24}	6.65×10^{-24}
SPT-CL J0257-6050	1.02×10^{-24}	8.46×10^{-24}
SPT-CL J0659-5300	1.30×10^{-24}	7.16×10^{-24}
SPT-CL J2145-4348	1.16×10^{-24}	6.94×10^{-24}
SPT-CL J0253-6046	1.24×10^{-24}	8.60×10^{-24}
SPT-CL J2302-4435	9.12×10^{-25}	7.40×10^{-24}
SPT-CL J2245-6206	1.48×10^{-24}	6.88×10^{-24}
SPT-CL J0337-4928	1.11×10^{-24}	8.30×10^{-24}
SPT-CL J2232-5959	1.93×10^{-24}	7.02×10^{-24}
SPT-CL J2040-5342	1.38×10^{-24}	6.60×10^{-24}
SPT-CL J0559-5249	1.42×10^{-24}	8.70×10^{-24}
SPT-CL J0307-6225	1.20×10^{-24}	7.45×10^{-24}
SPT-CL J0025-4133	1.80×10^{-24}	6.20×10^{-24}
SPT-CL J0109-4045	1.25×10^{-24}	8.90×10^{-24}
SPT-CL J0238-4904	1.70×10^{-24}	7.60×10^{-24}
SPT-CL J0221-4446	1.05×10^{-24}	6.50×10^{-24}
SPT-CL J2051-6256	1.60×10^{-24}	8.14×10^{-24}
SPT-CL J0218-4315	1.66×10^{-24}	7.76×10^{-24}
SPT-CL J0106-5355	1.40×10^{-24}	9.16×10^{-24}
SPT-CL J0219-4934	2.56×10^{-24}	8.45×10^{-24}
SPT-CL J0111-5518	3.20×10^{-24}	9.68×10^{-24}
SPT-CL J0351-4109	4.55×10^{-24}	9.06×10^{-24}
SPT-CL J2017-6258	2.76×10^{-24}	8.80×10^{-24}
SPT-CL J2148-6116	5.10×10^{-24}	9.85×10^{-24}
SPT-CL J0619-5802	3.88×10^{-24}	8.56×10^{-24}
SPT-CL J0135-5902	4.32×10^{-24}	9.20×10^{-24}
SPT-CL J0041-5107	2.44×10^{-24}	9.44×10^{-24}
SPT-CL J0342-5354	3.66×10^{-24}	9.00×10^{-24}
SPT-CL J0135-5904	5.66×10^{-24}	9.37×10^{-24}
SPT-CL J0343-5518	4.00×10^{-24}	8.10×10^{-24}

TABLE III – continued

SPT-CL J0033-6326	3.12×10^{-24}	9.75×10^{-24}
SPT-CL J0212-4657	5.22×10^{-24}	8.34×10^{-24}
SPT-CL J0410-6343	2.90×10^{-24}	9.54×10^{-24}
SPT-CL J0336-4005	4.78×10^{-24}	9.02×10^{-24}
SPT-CL J0217-4310	3.56×10^{-24}	8.68×10^{-24}
SPT-CL J2218-4519	2.10×10^{-24}	9.10×10^{-24}
SPT-CL J0429-5233	5.90×10^{-24}	9.88×10^{-24}
SPT-CL J2337-5942	4.20×10^{-24}	8.20×10^{-24}
SPT-CL J2155-6048	3.45×10^{-24}	9.30×10^{-24}
SPT-CL J2350-5301	2.60×10^{-24}	8.63×10^{-24}
SPT-CL J0542-4100	5.35×10^{-24}	9.45×10^{-24}
SPT-CL J2222-4834	4.04×10^{-24}	9.02×10^{-24}
SPT-CL J0522-5026	4.00×10^{-24}	8.79×10^{-24}
SPT-CL J0309-4958	2.84×10^{-24}	9.53×10^{-24}
SPT-CL J0202-5401	5.00×10^{-24}	8.91×10^{-24}
SPT-CL J0426-5455	4.68×10^{-24}	9.34×10^{-24}
SPT-CL J0142-5032	3.30×10^{-24}	8.50×10^{-24}
SPT-CL J0402-6130	2.34×10^{-24}	9.70×10^{-24}
SPT-CL J0011-4614	5.45×10^{-24}	8.76×10^{-24}
SPT-CL J2155-5224	4.12×10^{-24}	9.18×10^{-24}
SPT-CL J0444-4352	3.78×10^{-24}	8.12×10^{-24}
SPT-CL J2020-6314	3.00×10^{-24}	9.60×10^{-24}
SPT-CL J0030-5213	5.88×10^{-24}	8.90×10^{-24}
SPT-CL J0512-5139	4.55×10^{-24}	9.83×10^{-24}
SPT-CL J0152-5303	3.22×10^{-24}	8.48×10^{-24}
SPT-CL J2206-5807	2.72×10^{-24}	9.04×10^{-24}
SPT-CL J0157-4007	5.71×10^{-24}	9.25×10^{-24}
SPT-CL J0649-4510	4.36×10^{-24}	8.39×10^{-24}
SPT-CL J0543-4250	3.90×10^{-24}	9.77×10^{-24}
SPT-CL J2110-5244	2.50×10^{-24}	8.66×10^{-24}
SPT-CL J0243-5930	5.15×10^{-24}	9.40×10^{-24}
SPT-CL J0217-5014	4.84×10^{-24}	9.00×10^{-24}
SPT-CL J0256-5617	3.60×10^{-24}	9.15×10^{-24}
SPT-CL J2312-4621	2.15×10^{-24}	8.26×10^{-24}
SPT-CL J2354-5633	5.03×10^{-24}	9.50×10^{-24}
SPT-CL J2220-4534	4.28×10^{-24}	8.34×10^{-24}
SPT-CL J0519-4248	3.86×10^{-24}	9.82×10^{-24}
SPT-CL J0422-5140	2.66×10^{-24}	8.70×10^{-24}
SPT-CL J2140-5331	5.80×10^{-24}	1.45×10^{-23}
SPT-CL J2146-5736	4.10×10^{-24}	2.67×10^{-23}
SPT-CL J0334-4815	5.55×10^{-24}	3.12×10^{-23}
SPT-CL J0148-4518	7.56×10^{-24}	1.98×10^{-23}
SPT-CL J2146-4846	6.02×10^{-24}	2.34×10^{-23}
SPT-CL J0123-4821	6.60×10^{-24}	3.85×10^{-23}
SPT-CL J0145-4426	7.80×10^{-24}	2.19×10^{-23}
SPT-CL J2317-4707	7.20×10^{-24}	1.76×10^{-23}
SPT-CL J0352-5647	5.77×10^{-24}	3.54×10^{-23}
SPT-CL J0231-5403	7.76×10^{-24}	2.48×10^{-23}
SPT-CL J0231-4427	8.72×10^{-24}	1.09×10^{-23}
SPT-CL J2109-5040	6.72×10^{-24}	3.40×10^{-23}
SPT-CL J0615-5746	5.68×10^{-24}	2.92×10^{-23}
SPT-CL J0511-5154	6.35×10^{-24}	1.66×10^{-23}
SPT-CL J0307-4123	6.90×10^{-24}	3.00×10^{-23}
SPT-CL J0216-4219	6.94×10^{-24}	1.88×10^{-23}
SPT-CL J0612-4317	5.26×10^{-24}	2.75×10^{-23}
SPT-CL J2118-5055	5.45×10^{-24}	3.78×10^{-23}
SPT-CL J0622-4645	8.38×10^{-24}	1.22×10^{-23}
SPT-CL J0341-6143	7.80×10^{-24}	2.88×10^{-23}
SPT-CL J0049-5315	7.67×10^{-24}	3.68×10^{-23}
SPT-CL J0000-5748	7.70×10^{-24}	1.16×10^{-23}
SPT-CL J0014-4952	7.36×10^{-24}	2.55×10^{-23}
SPT-CL J0521-5104	7.06×10^{-24}	3.30×10^{-23}
SPT-CL J0233-5819	7.82×10^{-24}	2.05×10^{-23}
SPT-CL J2134-4109	5.36×10^{-24}	3.95×10^{-23}

TABLE III – continued

SPT-CL J0359-5218	7.00×10^{-24}	1.30×10^{-23}
SPT-CL J0528-4417	8.24×10^{-24}	2.40×10^{-23}
SPT-CL J0021-4902	7.90×10^{-24}	3.25×10^{-23}
SPT-CL J0310-4647	6.56×10^{-24}	1.57×10^{-23}
SPT-CL J2043-5035	5.82×10^{-24}	2.10×10^{-23}
SPT-CL J0324-6236	8.50×10^{-24}	3.06×10^{-23}
SPT-CL J0441-4855	7.93×10^{-24}	1.82×10^{-23}
SPT-CL J0406-4805	6.90×10^{-24}	2.99×10^{-23}
SPT-CL J2358-4354	6.63×10^{-24}	3.44×10^{-23}
SPT-CL J0230-6028	5.35×10^{-24}	1.08×10^{-23}
SPT-CL J2259-6057	6.68×10^{-24}	2.66×10^{-23}
SPT-CL J2034-5936	5.75×10^{-24}	3.17×10^{-23}
SPT-CL J0103-4250	5.46×10^{-24}	2.00×10^{-23}
SPT-CL J0118-5156	6.16×10^{-24}	2.82×10^{-23}
SPT-CL J0449-4901	8.10×10^{-24}	3.50×10^{-23}
SPT-CL J2106-4421	7.18×10^{-24}	1.65×10^{-23}
SPT-CL J0131-5604	6.04×10^{-24}	2.77×10^{-23}
SPT-CL J0641-4733	6.65×10^{-24}	3.90×10^{-23}
SPT-CL J2258-4044	6.25×10^{-24}	1.12×10^{-23}
SPT-CL J2301-4023	6.16×10^{-24}	2.64×10^{-23}
SPT-CL J0058-6145	6.84×10^{-24}	3.38×10^{-23}
SPT-CL J2146-4633	7.96×10^{-24}	1.48×10^{-23}
SPT-CL J0646-6236	7.72×10^{-24}	2.20×10^{-23}
SPT-CL J2106-5844	7.40×10^{-24}	3.73×10^{-23}
SPT-CL J2341-5119	8.85×10^{-24}	3.45×10^{-23}

A. Combined Upper limits from all clusters

We constructed the likelihood profiles for each individual cluster and then summed them to calculate a cumulative limit on the annihilation cross-section. This process is applied to all 350 clusters, both including and excluding those with $\text{TS} > 4$. We use the same methodology as described in [31, 93]. As shown in Fig. 7, we first include all 350 clusters and present the annihilation cross-section limits for the $b\bar{b}$ as well as $\tau^+\tau^-$ channel. Next, we exclude the clusters with $\text{TS} > 4$, viz. SPT-CL J2012-5649, SPT-CL J2300-5331, SPT-CL J2021-5257 and SPT-CL J0124-5937 and recalculate the upper limits which are superposed in Fig. 7. The inclusion of high-significance clusters introduces an excess signal, which somewhat biases the cross-section limits towards higher values. However, the combined limits are still roughly of the same order of magnitude.

VII. CONCLUSIONS

In this work, we searched for gamma-ray emission between 1 and 300 GeV from dark matter annihilation in galaxy clusters. We analyzed 350 clusters selected from the SPT-SZ 2500 square degree survey, which provides a mass-limited sample. The analysis utilized 15.7 years of data from the Fermi-LAT telescope and employed the DMFIT template. Notably, we identified a 3σ signal from the galaxy cluster SPT-CL J2021-5257. The best fit value of $\langle\sigma v\rangle$ for SPT-CL J2021-5257 is found to be $(6.0 \pm 0.6) \times 10^{-25} \text{ cm}^3\text{s}^{-1}$ and the best fit WIMP mass as 60.0 ± 11.8 GeV for the $b\bar{b}$ annihilation channel. For the $\tau^+\tau^-$ annihilation channel, we found the best-fit value as $\langle\sigma v\rangle = 3.5 \pm 0.9 \times 10^{-25} \text{ cm}^3\text{s}^{-1}$ and best-fit WIMP mass as 15.3 ± 4.1 GeV. The TS map for this cluster can be found in Fig. 2. Although prima-facie, we found 3σ detection evidence from SPT-CL J2021-5257, the estimated annihilation cross-section is in conflict with upper limits from Milky way dwarf spheroidal galaxies. Therefore, we conclude that the enhanced signal seen for SPT-CL J2021-5257 cannot be due to dark matter annihilation. Furthermore, if we consider the look elsewhere effect the global p -value for this cluster is consistent with the expected background. We also obtained a marginal significance of around 2σ for three other clusters: SPT-CL J2012-5649, SPT-CL J0124-5937, and SPT-CL J2300-5331. All the remaining clusters showed null results and the TS values were consistent with background.

Therefore, we then calculate upper limits for all the analyzed clusters. Among the clusters with $> 2\sigma$ significance we found the most stringent limit for SPT-CL J2300-5331, viz. $\langle\sigma v\rangle = 8.85 \times 10^{-26} \text{ cm}^3\text{s}^{-1}$ for $m_\chi = 10$ GeV and $b\bar{b}$ annihilation channel and $\langle\sigma v\rangle = 10.0 \times 10^{-26} \text{ cm}^3\text{s}^{-1}$ for $m_\chi = 10$ GeV and $\tau^+\tau^-$ annihilation

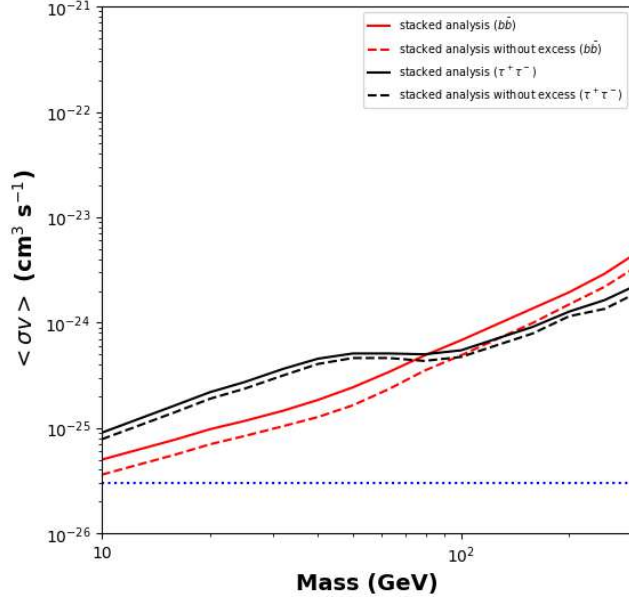


FIG. 7: 95% CL upper limits on the annihilation cross-section for the $b\bar{b}$ (red) and $\tau^+\tau^-$ (black) annihilation channels using the combined data from all clusters. The solid lines represent the results for all 350 clusters, while dashed lines show the limits when clusters with $\text{TS} > 4$, viz, SPT-CL J2012-5649, SPT-CL J2300-5331, SPT-CL J2021-5257 and SPT-CL J0124-5937 are excluded. The dotted blue line shows the canonical thermal cross-section of $3 \times 10^{-26} \text{ cm}^3 \text{s}^{-1}$.

channel at 95% c.l. Among all the remaining clusters, the most stringent upper limits for annihilation to $b\bar{b}$ is obtained for SPT-CL J0455-4159, as $\langle \sigma v \rangle = 6.44 \times 10^{-26} \text{ cm}^3 \text{s}^{-1}$ for $m_\chi = 10 \text{ GeV}$ for $b\bar{b}$ annihilation channel, and $\langle \sigma v \rangle = 8.26 \times 10^{-26} \text{ cm}^3 \text{s}^{-1}$ for $m_\chi = 10 \text{ GeV}$ for $\tau^+\tau^-$ annihilation channel at 95% c.l. We also show the combined upper limits for all the clusters in Fig. 7. In the Appendices, we also check the robustness of our results by redoing the analysis with different assumptions for the dark matter substructure and log-normal uncertainties on the J -factor.

Moving forward, we plan to expand this analysis to encompass all galaxy clusters detected in ongoing X-ray and SZ surveys such as eROSITA [94] and SPTPol [95].

Acknowledgments

We are grateful to the Fermi-LAT and CLUMPY teams for their invaluable contributions in making the data and analysis codes publicly available. Their expertise and willingness to answer our queries were instrumental in this research. This work was motivated after a stimulating talk by Mattia Di Mauro at IIT Hyderabad. We also thank the anonymous referee for useful constructive feedback on our manuscript. We also acknowledge the National Supercomputing Mission (NSM) for providing essential computing resources on the ‘PARAM SEVA’ supercomputer at IIT Hyderabad. This initiative is implemented by C-DAC and supported by the Ministry of Electronics and Information Technology (MeitY) and the Department of Science and Technology (DST) of the Government of India. Finally, we thank the Smithsonian Astrophysical Observatory for developing SAOImageDS9, which played a valuable role in our analysis.

-
- [1] G. Jungman, M. Kamionkowski, and K. Griest, Physics Reports **267**, 195 (1996), hep-ph/9506380.
 - [2] G. Bertone, D. Hooper, and J. Silk, Physics Reports **405**, 279 (2005), hep-ph/0404175.
 - [3] G. Bertone and D. Hooper, Reviews of Modern Physics **90**, 045002 (2018), 1605.04909.
 - [4] A. Bosma, arXiv e-prints arXiv:2309.06390 (2023), 2309.06390.
 - [5] Planck Collaboration, N. Aghanim, Y. Akrami, M. Ashdown, J. Aumont, C. Baccigalupi, M. Ballardini, A. J. Banday, R. B. Barreiro, N. Bartolo, et al., Astron. & Astrophys. **641**, A6 (2020), 1807.06209.
 - [6] B. W. Lee and S. Weinberg, Phys. Rev. Lett. **39**, 165 (1977).
 - [7] J. Ellis, J. S. Hagelin, D. V. Nanopoulos, K. Olive, and M. Srednicki, Nuclear Physics B **238**, 453 (1984).
 - [8] G. Steigman, B. Dasgupta, and J. F. Beacom, Phys. Rev. D **86**, 023506 (2012), 1204.3622.
 - [9] M. Schumann, Journal of Physics G Nuclear Physics **46**, 103003 (2019), 1903.03026.

- [10] Y. B. Zeldovich, A. Klypin, M. Y. Khlopov, and V. M. Chechetkin, Soviet Journal of Nuclear Physics **31**, 664 (1980).
- [11] M. Cirelli, Pramana **79**, 1021 (2012), 1202.1454.
- [12] F. Donato, Physics of the Dark Universe **4**, 41 (2014).
- [13] S. Desai, Y. Ashie, S. Fukuda, Y. Fukuda, K. Ishihara, Y. Itow, Y. Koshio, A. Minamino, M. Miura, S. Moriyama, et al., Phys. Rev. D **70**, 083523 (2004), hep-ex/0404025.
- [14] I. Cholis, D. P. Finkbeiner, L. Goodenough, and N. Weiner, JCAP **2009**, 007 (2009), 0810.5344.
- [15] J. Heisig, Modern Physics Letters A **36**, 2130003-414 (2021), 2012.03956.
- [16] M. H. Chan, Galaxies **9**, 11 (2021).
- [17] S. Funk, Proceedings of the National Academy of Science **112**, 12264 (2015), 1310.2695.
- [18] A. Boveia and C. Doglioni, Annual Review of Nuclear and Particle Science **68**, 429 (2018), 1810.12238.
- [19] A. V. Kravtsov and S. Borgani, Ann. Rev. Astron. Astrophys. **50**, 353 (2012), 1205.5556.
- [20] S. W. Allen, A. E. Evrard, and A. B. Mantz, Ann. Rev. Astron. Astrophys. **49**, 409 (2011), 1103.4829.
- [21] A. A. Vikhlinin, A. V. Kravtsov, M. L. Markevich, R. A. Sunyaev, and E. M. Churazov, Physics Uspekhi **57**, 317-341 (2014).
- [22] H. Böhringer and G. Chon, Modern Physics Letters A **31**, 1640008 (2016), 1610.02855.
- [23] S. Desai, Physics Letters B **778**, 325 (2018), 1708.06502.
- [24] K. Bora and S. Desai, JCAP **2021**, 012 (2021), 2008.10541.
- [25] K. Bora and S. Desai, JCAP **2021**, 052 (2021), 2104.00974.
- [26] K. Bora, R. F. L. Holanda, S. Desai, and S. H. Pereira, European Physical Journal C **82**, 17 (2022), 2106.15805.
- [27] S. Colafrancesco, S. Profumo, and P. Ullio, Astron. & Astrophys. **455**, 21 (2006), astro-ph/0507575.
- [28] W. B. Atwood, A. A. Abdo, M. Ackermann, W. Althouse, B. Anderson, M. Axelsson, L. Baldini, J. Ballet, D. L. Band, G. Barbiellini, et al., Astrophys. J. **697**, 1071 (2009), 0902.1089.
- [29] M. Ackermann, M. Ajello, A. Allafort, L. Baldini, J. Ballet, G. Barbiellini, D. Bastieri, K. Bechtol, R. Bellazzini, R. D. Blandford, et al., JCAP **2010**, 025 (2010), 1002.2239.
- [30] S. Ando and D. Nagai, JCAP **2012**, 017 (2012), 1201.0753.
- [31] X. Huang, G. Vertongen, and C. Weniger, JCAP **2012**, 042 (2012), 1110.1529.
- [32] J. Han, C. S. Frenk, V. R. Eke, L. Gao, S. D. M. White, A. Boyarsky, D. Malyshev, and O. Ruchayskiy, MNRAS **427**, 1651 (2012), 1207.6749.
- [33] A. Hektor, M. Raidal, and E. Tempel, Astrophys. J. Lett. **762**, L22 (2013), 1207.4466.
- [34] B. Anderson, S. Zimmer, J. Conrad, M. Gustafsson, M. Sánchez-Conde, and R. Caputo, JCAP **2016**, 026 (2016), 1511.00014.
- [35] Y.-F. Liang, Z.-Q. Shen, X. Li, Y.-Z. Fan, X. Huang, S.-J. Lei, L. Feng, E.-W. Liang, and J. Chang, Phys. Rev. D **93**, 103525 (2016), 1602.06527.
- [36] M. Ackermann, M. Ajello, A. Albert, W. B. Atwood, L. Baldini, G. Barbiellini, D. Bastieri, K. Bechtol, R. Bellazzini, E. Bissaldi, et al., Astrophys. J. **812**, 159 (2015), 1510.00004.
- [37] M. Lisanti, S. Mishra-Sharma, N. L. Rodd, and B. R. Safdi, Phys. Rev. Lett. **120**, 101101 (2018), 1708.09385.
- [38] C. Thorpe-Morgan, D. Malyshev, C.-A. Stegen, A. Santangelo, and J. Jochum, MNRAS **502**, 4039 (2021), 2010.11006.
- [39] Z.-Q. Shen, Z.-Q. Xia, and Y.-Z. Fan, Astrophys. J. **920**, 1 (2021), 2108.00363.
- [40] M. Di Mauro, J. Pérez-Romero, M. A. Sánchez-Conde, and N. Fornengo, Phys. Rev. D **107**, 083030 (2023), 2303.16930.
- [41] D. Song, N. Hiroshima, and K. Murase, arXiv e-prints arXiv:2401.15606 (2024), 2401.15606.
- [42] X. Tan, M. Colavincenzo, and S. Ammazzalorso, MNRAS **495**, 114 (2020), 1907.06905.
- [43] S. Murgia, Annual Review of Nuclear and Particle Science **70**, 455 (2020).
- [44] R. A. Sunyaev and Y. B. Zeldovich, Comments on Astrophysics and Space Physics **4**, 173 (1972).
- [45] S. Manna and S. Desai, JCAP **2024**, 017 (2024), 2310.07519.
- [46] J. E. Carlstrom, P. A. R. Ade, K. A. Aird, B. A. Benson, L. E. Bleem, S. Busetti, C. L. Chang, E. Chauvin, H. M. Cho, T. M. Crawford, et al., Pub. Astro. Soc. Pac. **123**, 568 (2011), 0907.4445.
- [47] L. E. Bleem, B. Stalder, T. de Haan, K. A. Aird, S. W. Allen, D. E. Applegate, M. L. N. Ashby, M. Bautz, M. Bayliss, B. A. Benson, et al., Astrophys. J. Suppl. Ser. **216**, 27 (2015), 1409.0850.
- [48] S. Bocquet, J. P. Dietrich, T. Schrabback, L. E. Bleem, M. Klein, S. W. Allen, D. E. Applegate, M. L. N. Ashby, M. Bautz, M. Bayliss, et al., Astrophys. J. **878**, 55 (2019), 1812.01679.
- [49] J. Song, A. Zenteno, B. Stalder, S. Desai, L. E. Bleem, K. A. Aird, R. Armstrong, M. L. N. Ashby, M. Bayliss, G. Bazin, et al., Astrophys. J. **761**, 22 (2012), 1207.4369.
- [50] J. Ruel, G. Bazin, M. Bayliss, M. Brodin, R. J. Foley, B. Stalder, K. A. Aird, R. Armstrong, M. L. N. Ashby, M. Bautz, et al., Astrophys. J. **792**, 45 (2014), 1311.4953.
- [51] S. Desai, R. Armstrong, J. J. Mohr, D. R. Semler, J. Liu, E. Bertin, S. S. Allam, W. A. Barkhouse, G. Bazin, E. J. Buckley-Geer, et al., Astrophys. J. **757**, 83 (2012), 1204.1210.
- [52] A. Saro, S. Bocquet, E. Rozo, B. A. Benson, J. Mohr, E. S. Rykoff, M. Soares-Santos, L. Bleem, S. Dodelson, P. Melchior, et al., MNRAS **454**, 2305 (2015), 1506.07814.
- [53] A. Charbonnier, C. Combet, and D. Maurin, Computer Physics Communications **183**, 656 (2012), 1201.4728.
- [54] V. Bonnivard, M. Hüttner, E. Nezri, A. Charbonnier, C. Combet, and D. Maurin, Computer Physics Communications **200**, 336 (2016), 1506.07628.
- [55] M. Hüttner, C. Combet, and D. Maurin, Computer Physics Communications **235**, 336 (2019), 1806.08639.
- [56] M. Cirelli, G. Corcella, A. Hektor, G. Hütsi, M. Kadastik, P. Panci, M. Raidal, F. Sala, and A. Strumia, JCAP **2011**, 051 (2011), 1012.4515.

- [57] A. B. Pace and L. E. Strigari, MNRAS **482**, 3480 (2019), 1802.06811.
- [58] F. Prada, A. A. Klypin, A. J. Cuesta, J. E. Betancort-Rijo, and J. Primack, MNRAS **423**, 3018 (2012), 1104.5130.
- [59] A. A. Klypin, S. Trujillo-Gomez, and J. Primack, Astrophys. J. **740**, 102 (2011), 1002.3660.
- [60] L. Gao, S. D. M. White, A. Jenkins, F. Stoehr, and V. Springel, MNRAS **355**, 819 (2004), astro-ph/0404589.
- [61] M. Kuhlen, M. Vogelsberger, and R. Angulo, Physics of the Dark Universe **1**, 50 (2012), 1209.5745.
- [62] J. Zavala and C. S. Frenk, Galaxies **7**, 81 (2019), 1907.11775.
- [63] J. F. Navarro, C. S. Frenk, and S. D. M. White, Astrophys. J. **462**, 563 (1996), astro-ph/9508025.
- [64] J. F. Navarro, C. S. Frenk, and S. D. M. White, Astrophys. J. **490**, 493 (1997), astro-ph/9611107.
- [65] H. Zhao, MNRAS **278**, 488 (1996), astro-ph/9509122.
- [66] L. E. Bleem, B. Stalder, T. de Haan, K. A. Aird, S. W. Allen, D. E. Applegate, M. L. N. Ashby, M. Bautz, M. Bayliss, B. A. Benson, et al., Astrophys. J. Suppl. Ser. **216**, 27 (2015), 1409.0850.
- [67] M. White, Astron. & Astrophys. **367**, 27 (2001), astro-ph/0011495.
- [68] M. A. Sánchez-Conde and F. Prada, MNRAS **442**, 2271 (2014), 1312.1729.
- [69] C. S. Frenk and S. D. M. White, Annalen der Physik **524**, 507 (2012), 1210.0544.
- [70] M. Hüttén, C. Combet, and D. Maurin, JCAP **2018**, 005 (2018), 1711.08323.
- [71] J. Einasto, Trudy Astrofizicheskogo Instituta Alma-Ata **5**, 87 (1965).
- [72] A. Aguirre-Santaella, M. A. Sánchez-Conde, G. Ogiya, J. Stückler, and R. E. Angulo, MNRAS **518**, 93 (2023), 2207.08652.
- [73] R. Errani and J. F. Navarro, MNRAS **505**, 18 (2021), 2011.07077.
- [74] V. Springel, J. Wang, M. Vogelsberger, A. Ludlow, A. Jenkins, A. Helmi, J. F. Navarro, C. S. Frenk, and S. D. M. White, MNRAS **391**, 1685 (2008), 0809.0898.
- [75] R. Errani and J. Peñarrubia, MNRAS **491**, 4591 (2020), 1906.01642.
- [76] S. Kazantzidis, J. Magorrian, and B. Moore, Astrophys. J. **601**, 37 (2004), astro-ph/0309517.
- [77] J. Peñarrubia, A. J. Benson, M. G. Walker, G. Gilmore, A. W. McConnachie, and L. Mayer, MNRAS **406**, 1290 (2010), 1002.3376.
- [78] Á. Moliné, M. A. Sánchez-Conde, S. Palomares-Ruiz, and F. Prada, MNRAS **466**, 4974 (2017), 1603.04057.
- [79] Á. Moliné, M. A. Sánchez-Conde, A. Aguirre-Santaella, T. Ishiyama, F. Prada, S. A. Cora, D. Croton, E. Jullo, R. B. Metcalf, T. Oogi, et al., MNRAS **518**, 157 (2023), 2110.02097.
- [80] O. Newton, N. I. Libeskind, A. Knebe, M. A. Sánchez-Conde, J. G. Sorce, S. Pilipenko, M. Steinmetz, R. Pakmor, E. Tempel, Y. Hoffman, et al., MNRAS **514**, 3612 (2022), 2104.11242.
- [81] M. Ackermann, M. Ajello, A. Albert, A. Allafort, W. B. Atwood, M. Axelsson, L. Baldini, J. Ballet, G. Barbiellini, D. Bastieri, et al., Astrophys. J. Suppl. Ser. **203**, 4 (2012), 1206.1896.
- [82] M. Ackermann, M. Ajello, W. B. Atwood, L. Baldini, J. Ballet, G. Barbiellini, D. Bastieri, K. Bechtol, R. Bellazzini, B. Berenji, et al., Astrophys. J. **750**, 3 (2012), 1202.4039.
- [83] W. Atwood, A. Albert, L. Baldini, M. Tinivella, J. Bregeon, M. Pesce-Rollins, C. Sgrò, P. Bruel, E. Charles, A. Drlica-Wagner, et al., arXiv e-prints arXiv:1303.3514 (2013), 1303.3514.
- [84] J. Ballet, P. Bruel, T. H. Burnett, B. Lott, and The Fermi-LAT collaboration, arXiv e-prints arXiv:2307.12546 (2023), 2307.12546.
- [85] M. Wood, R. Caputo, E. Charles, M. Di Mauro, J. Magill, J. S. Perkins, and Fermi-LAT Collaboration, in *35th International Cosmic Ray Conference (ICRC2017)* (2017), vol. 301 of *International Cosmic Ray Conference*, p. 824, 1707.09551.
- [86] T. E. Jeltema and S. Profumo, JCAP **2008**, 003 (2008), 0808.2641.
- [87] J. R. Mattox, D. L. Bertsch, J. Chiang, B. L. Dingus, S. W. Digel, J. A. Esposito, J. M. Fierro, R. C. Hartman, S. D. Hunter, G. Kanbach, et al., Astrophys. J. **461**, 396 (1996).
- [88] S. S. Wilks, Annals Math. Statist. **9**, 60 (1938).
- [89] V. Pasumarti and S. Desai, JCAP **2022**, 002 (2022), 2210.12804.
- [90] S. Manna and S. Desai, JCAP **2024**, 013 (2024), 2401.13240.
- [91] M. Di Mauro and M. W. Winkler, Phys. Rev. D **103**, 123005 (2021), 2101.11027.
- [92] E. Gross and O. Vitells, European Physical Journal C **70**, 525 (2010), 1005.1891.
- [93] A. McDaniel, M. Ajello, C. M. Karwin, M. Di Mauro, A. Drlica-Wagner, and M. A. Sánchez-Conde, Phys. Rev. D **109**, 063024 (2024), 2311.04982.
- [94] M. Kluge, J. Comparat, A. Liu, F. Balzer, E. Bulbul, J. Ider Chitham, V. Ghirardini, C. Garrel, Y. E. Bahar, E. Artis, et al., arXiv e-prints arXiv:2402.08453 (2024), 2402.08453.
- [95] L. E. Bleem, M. Klein, T. M. C. Abbot, P. A. R. Ade, M. Aguena, O. Alves, A. J. Anderson, F. Andrade-Oliveira, B. Ansarinejad, M. Archipley, et al., The Open Journal of Astrophysics **7**, 13 (2024), 2311.07512.
- [96] R. Bartels and S. Ando, Phys. Rev. D **92**, 123508 (2015), 1507.08656.
- [97] L. Gao, C. S. Frenk, A. Jenkins, V. Springel, and S. D. M. White, MNRAS **419**, 1721 (2012), 1107.1916.

Appendix A: Boost Factor using different subhalo models

In addition to calculating the boost factors using the subhalo model discussed in the main manuscript, we followed the conservative models for the subhalo outlined in [96] and the more aggressive model defined in [97], and calculated the boost factor as a function of minimum subhalo mass for all the four clusters with significance $> 2\sigma$. The conservative model in [96] uses two different *ansatzes* for the subhalo mass function obtained from

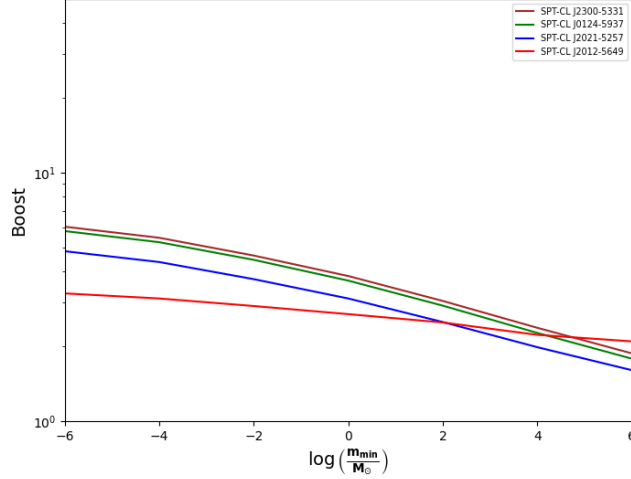


FIG. 8: The boost as a function of the minimum subhalo mass for all four clusters with significance $>2\sigma$ using the subhalo mass function from [68] with Power Law Index -1.9. The methodology followed is similar to [96].

[68]. The first subhalo mass function considered is given by $\frac{dN}{dm} = \frac{0.03}{M} \left(\frac{m}{M}\right)^{-1.9}$, where $\frac{dN}{dm}$ describes the number density of subhalos per unit mass m within a host halo of mass M . For SPT-CL J2021-5257, we obtained a J -factor of 2.30×10^{16} and a TS value of 8.5 using this model. The second subhalo mass function used in [96] is given by $\frac{dN}{dm} = \frac{0.012}{M} \left(\frac{m}{M}\right)^{-2.0}$, for which the J -factor increased to 2.15×10^{17} and the TS to 10.7 for this cluster. We then considered the aggressive model for the subhalo profile [97], which adopted the results from high-resolution simulations of galaxy cluster haloes (the Phoenix Project). Using this aggressive model, we found a J -factor of 3.13×10^{18} and a TS of 11.5 for SPT-CL J2021-5257. These J -factor values correspond to a minimum subhalo mass of $10^{-6} M_\odot$. We then redid the same exercise for three other clusters with significance $> 2\sigma$ and report the J -Factors and TS values in Table IV. The boost factors as a function of the minimum halo mass can be found in Figures 8, 9 and 10 respectively. Despite using these different boost factors, we do not find any cluster with TS > 25 .

TABLE IV: J -Factors and TS values for four clusters (with TS > 4) using three different methods for subhalo mass distributions and $b\bar{b}$ annihilation channel. The first two columns represent the conservative models described in [96], and the other one is a more aggressive model defined in [97].

Cluster	[96] with Power Law Index -1.9		[96] with Power Law Index -2.0		[97]	
	J -Factor [GeV 2 cm $^{-5}$]	TS	J -Factor [GeV 2 cm $^{-5}$]	TS	J -Factor [GeV 2 cm $^{-5}$]	TS
SPT-CL J2021-5257	2.30×10^{16}	8.50	2.15×10^{17}	10.70	3.13×10^{18}	11.50
SPT-CL J2012-5649	5.90×10^{16}	6.00	2.10×10^{17}	7.20	4.70×10^{18}	7.70
SPT-CL J0124-5937	1.42×10^{16}	3.70	4.77×10^{16}	4.55	2.35×10^{18}	5.00
SPT-CL J2300-5331	1.18×10^{16}	4.35	7.56×10^{16}	5.65	1.77×10^{18}	6.20

Appendix B: Best-Fit WIMP parameters using different subhalo models

We now recalculate the best-fit values of mass and annihilation cross-section using the conservative subhalo models defined in [96] and the aggressive model in [97], as discussed in Appendix A. The best-fit values for the WIMP mass and annihilation cross-section for all the four clusters with TS > 4 can be found in Table V for both $b\bar{b}$ and $\tau^+\tau^-$ annihilation channels. All the best-fit values for the annihilation cross-section are $\mathcal{O}(10^{-25} - 10^{-24})$ cm 3 s $^{-1}$. Therefore, the new best-fit values are still in conflict with the upper limits from dwarf spheroidal galaxies [91]. Among the clusters with TS > 4 , the lowest value for the best-fit annihilation cross-section was obtained for SPT-CL J2300-5331 using the aggressive model defined in [97]. For the $b\bar{b}$ annihilation channel, this best-fit value is equal to $\langle\sigma v\rangle = (9.3 \pm 0.4) \times 10^{-26}$ cm 3 s $^{-1}$, with a dark matter particle mass of $m_\chi = (52.6 \pm 3.7)$ GeV. For the $\tau^+\tau^-$ annihilation channel, the corresponding best-fit cross-section is $\langle\sigma v\rangle = (8.8 \pm 0.2) \times 10^{-26}$ cm 3 s $^{-1}$, with a WIMP mass of $m_\chi = (18.8 \pm 2.5)$ GeV. Di Mauro and Winkler [91] obtained a 95% upper limit for the annihilation cross-section of dark matter particles on Dwarf spheroidal galaxies, of

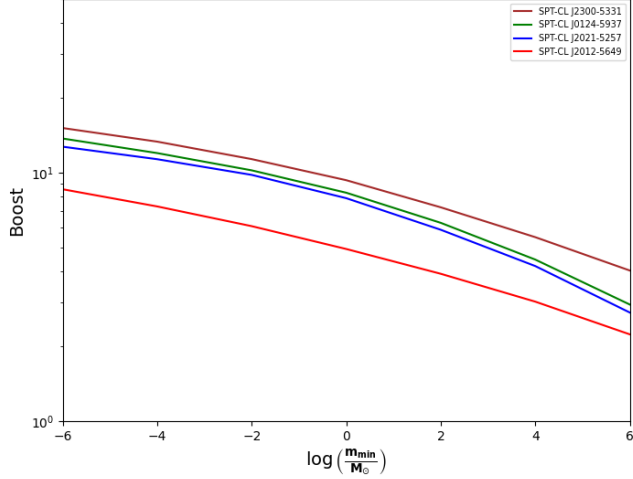


FIG. 9: Same as Fig. 8 but here we use power law index as -2.0.

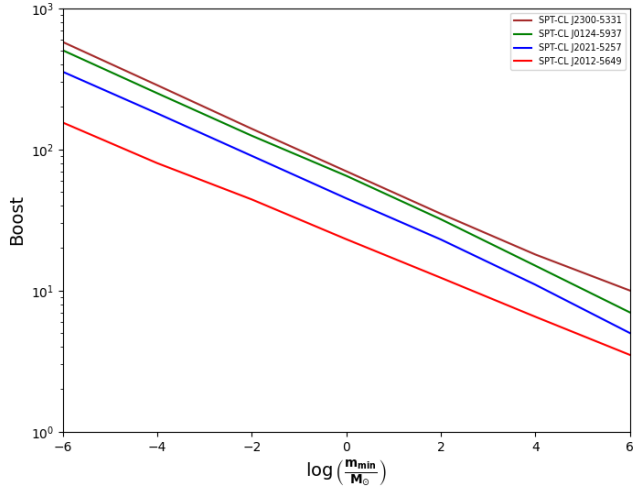


FIG. 10: Same as Fig. 8 but here we followed the subhalo model described in [97].

$\langle\sigma v\rangle = 1.5 \times 10^{-26} \text{ cm}^3 \text{s}^{-1}$ for the $b\bar{b}$ annihilation channel for WIMP mass of $m_\chi = 50$ GeV. For the $\tau^+\tau^-$ annihilation channel, the corresponding 95% upper limit is $\langle\sigma v\rangle = 9 \times 10^{-27} \text{ cm}^3 \text{s}^{-1}$ for WIMP mass of $m_\chi = 20$ GeV. Therefore, the lowest values of the annihilation cross-section which we obtain using the most aggressive halo models are still in tension with the upper limits from dwarf spheroidal galaxies at the best-fit WIMP mass which we found.

Appendix C: Statistical uncertainty in the J -factor

In our earlier analysis, we had not included the uncertainty in the central halo J -Factor. To account for this, we include a log-Gaussian uncertainty similar to Eq. 7 in [93] and Eq. 16 in D23. We include the statistical uncertainty on the J -factor by multiplying the Fermi-LAT binned Poisson likelihood function with a J -factor likelihood function that takes the form of a Gaussian in $\log_{10}(J)$ with width σ_i as described below:

$$L_i(J_i | J_{\text{obs},i}, \sigma_i) = \frac{1}{\log(10)J_{\text{obs},i}\sqrt{2\pi}\sigma_i} \times \exp \left[- \left(\frac{\log_{10}(J_i) - \log_{10}(J_{\text{obs},i})}{\sqrt{2}\sigma_i} \right)^2 \right] \quad (\text{C1})$$

The best-fit observed J -factor for the i^{th} cluster is denoted by $J_{\text{obs},i}$, and the error in $\log_{10}(J_{\text{obs},i})$ is denoted by σ_i . The value of the J -factor for which the likelihood is computed is represented by J_i . We considered three different values of σ_i , viz. 0.2, 0.4, and 0.6 dex similar to D23 and [93]. For galaxy clusters, the uncertainty due to substructure and mass-concentration relation has been estimated to be 0.2 in D23, whereas for dwarf

TABLE V: The best-fit mass and annihilation cross section for four clusters with $\text{TS} > 4$ for both $b\bar{b}$ and $\tau^+\tau^-$ annihilation channels using three different models. The first two columns represent the conservative models described in [96], and the other one is a more aggressive model defined in [97].

Cluster	$b\bar{b}$ Channel					
	[96] with Power Law Index -1.9		[96] with Power Law Index -2.0		[97]	
	m_x (GeV)	$\langle\sigma v\rangle$ ($\text{cm}^3 \text{s}^{-1}$)	m_x (GeV)	$\langle\sigma v\rangle$ ($\text{cm}^3 \text{s}^{-1}$)	m_x (GeV)	$\langle\sigma v\rangle$ ($\text{cm}^3 \text{s}^{-1}$)
SPT-CL J2021-5257	78.3 ± 7.5	$(2.4 \pm 0.5) \times 10^{-24}$	55.8 ± 4.5	$(5.1 \pm 0.4) \times 10^{-25}$	48.3 ± 4.7	$(2.5 \pm 0.9) \times 10^{-25}$
SPT-CL J2012-5649	105.8 ± 11.1	$(8.0 \pm 0.7) \times 10^{-24}$	80.3 ± 3.7	$(4.7 \pm 0.5) \times 10^{-24}$	72.8 ± 5.1	$(9.8 \pm 0.5) \times 10^{-25}$
SPT-CL J0124-5937	62.3 ± 3.4	$(2.7 \pm 1.3) \times 10^{-24}$	35.7 ± 6.1	$(5.5 \pm 0.7) \times 10^{-25}$	29.0 ± 3.5	$(3.0 \pm 0.7) \times 10^{-25}$
SPT-CL J2300-5331	73.9 ± 4.7	$(6.1 \pm 0.8) \times 10^{-25}$	58.0 ± 4.2	$(2.1 \pm 0.3) \times 10^{-25}$	52.6 ± 3.7	$(9.3 \pm 0.4) \times 10^{-26}$
Cluster	$\tau^+\tau^-$ Channel					
	[96] with Power Law Index -1.9		[96] with Power Law Index -2.0		[97]	
	m_x (GeV)	$\langle\sigma v\rangle$ ($\text{cm}^3 \text{s}^{-1}$)	m_x (GeV)	$\langle\sigma v\rangle$ ($\text{cm}^3 \text{s}^{-1}$)	m_x (GeV)	$\langle\sigma v\rangle$ ($\text{cm}^3 \text{s}^{-1}$)
SPT-CL J2021-5257	27.4 ± 2.3	$(7.8 \pm 1.2) \times 10^{-25}$	13.4 ± 2.5	$(2.5 \pm 0.4) \times 10^{-25}$	10.7 ± 1.3	$(1.8 \pm 0.3) \times 10^{-25}$
SPT-CL J2012-5649	33.1 ± 1.8	$(7.2 \pm 0.6) \times 10^{-24}$	21.7 ± 0.8	$(3.7 \pm 0.5) \times 10^{-24}$	19.5 ± 1.8	$(7.5 \pm 0.5) \times 10^{-25}$
SPT-CL J0124-5937	24.0 ± 3.1	$(1.8 \pm 1.0) \times 10^{-24}$	12.9 ± 2.1	$(4.5 \pm 0.7) \times 10^{-25}$	11.0 ± 1.5	$(2.7 \pm 0.6) \times 10^{-25}$
SPT-CL J2300-5331	25.7 ± 3.0	$(5.3 \pm 0.7) \times 10^{-25}$	20.3 ± 2.7	$(1.1 \pm 0.3) \times 10^{-25}$	18.8 ± 2.5	$(8.8 \pm 0.2) \times 10^{-26}$

galaxies, it is about 0.6 dex [93]. D23 also did the analysis for $\sigma_i = 0.4$ dex. Therefore, we considered all the three values of σ_i . Nevertheless, D23 has shown that the best-fit values for the WIMP mass and annihilation cross-section are not affected by σ_i .

We then proceed to calculate TS values for all the four clusters with TS values > 4 , after accounting for log-Gaussian uncertainty in the J -Factors using all the three values of σ_i and report them in Table VI. The results for TS are not much different compared to the earlier values and we still do not find any cluster with $\text{TS} > 25$. There is also not much difference in the new TS values compared to the previous values which did not assume any uncertainty on σ_i .

TABLE VI: J -Factors including statistical uncertainty and TS values for clusters with significance $> 2\sigma$ for the $b\bar{b}$ annihilation channel. We show the values for three different values of σ_i . For comparison we have also shown the J -Factors and TS values without including the uncertainty.

Cluster Name	$\log_{10}(J)$ without σ_i [$\log_{10}\text{GeV}^2 \text{cm}^{-5}$]	TS Values without σ_i	σ_i [dex]	TS Values
SPT-CL J2021-5257	16.40	9.00	0.20	9.35
			0.40	9.70
			0.60	10.20
SPT-CL J2012-5649	16.79	6.20	0.20	6.85
			0.40	7.10
			0.60	7.20
SPT-CL J0124-5937	16.26	4.00	0.20	4.15
			0.40	4.50
			0.60	4.73
SPT-CL J2300-5331	16.14	4.60	0.20	4.77
			0.40	5.00
			0.60	5.30